Journal of Molecular Modeling (2025) 31:168
https://doi.org/10.1007/s00894-025-06378-9

ORIGINAL PAPER

The $\alpha/\beta3$ complex of human voltage-gated sodium channel hNa$_v$1.7 to study mechanistic differences in presence and absence of auxiliary subunit $\beta3$

Jordan Edilberto Ruiz-Castelan[1] · **Fernando Villa-Díaz**[2] · **María Eugenia Castro**[3] · **Francisco J. Melendez**[4] · **Thomas Scior**[1]

Received: 3 December 2024 / Accepted: 25 April 2025
© The Author(s) 2025

Abstract

Context In the context of structural interactomics, we generated a 3D model between α and β3 subunits for the hitherto unknown human voltage-gated sodium channel complex (hNa 1.7α/β3). We embedded our 3D model in a membrane lipid bilayer for molecular dynamics (MD) simulations of the sodium cation passage from the outer vestibule through the inner pore segment of our hNa 1.7 complex in presence and absence of auxiliary subunit β3 with remarkable changes close to electrophysiological study results. A complete passage could not be expected due to because the inactivated state of the underlying 3D template. A complete sodium ion passage would require an open state of the channel. The computed observations concerning side chain rearrangements for favorable cooperativity under evolutionary neighborhood conditions, favorable and unfavorable amino acid interactions, proline kink, loop, and helix displacements were all found in excellent keeping with the extant literature without any exception nor contradiction. Complex-stabilizing pairs of interacting amino acids with evolutionary neighborhood complementary were identified.

Methods The following tools were used: sequence search and alignment by FASTA and Clustal Omega; 3D model visualization and homology modeling by Vega ZZ, SPDBV, Chimera and Modeller, respectively; missing sections (loops) by Alphafold; geometry optimization prior to MD runs by GROMACS 2021.4 under the CHARMM 36 force field; local healing of bad contacts by SPDBV based on its Ramachandran plots; protein-protein docking by HDOCK 2.4; membrane insertion assisted by OPM; Berendsen V-rescaling for NVT; Parrinello-Rahman and Nose-Hoover for MPT; MD analyses by VMD and XMGRACE

Keywords Sodium channel hNa$_v$1.7 · Molecular dynamics simulations · Molecular docking · Three-dimensional model · Protein–protein interfaces

Introduction

The human voltage-gated sodium channel (hNa$_v$) is subdivided into nine channel subtypes by their alpha (α) subunit (hNa$_v$ 1.1 to 1.9). In the case of our target channel hNa$_v$1.7, small organic compounds have been reported which modify its gating kinetics [1]. The channel constitutes a multisubunit complex, and its presence in the cell membrane is required for vital electrophysiological Na$^+$ influx and depolarization processes [2–4]. While the central membrane-spanning α subunit comprises the pore, the beta (β) subunit behaves also as a channel activity modulator. The central unit is formed by four domains (DI–DIV) and each domain is made up of six transmembrane segments (S1-S6). The manner of distribution/folding allows the VSD voltage-sensing domains to form and be made up of the S1–S4 segments

✉ Francisco J. Melendez
francisco.melendez@correo.buap.mx

✉ Thomas Scior
thomas.scior@correo.buap.mx

[1] Laboratory of Computational Molecular Simulations, Faculty of Chemical Sciences, BUAP, C.P. 72570 Puebla, Mexico

[2] Laboratory of Basical Science, Tecnologico Nacional de Mexico, Campus Guaymas, C.P. 85480 Sonora, Mexico

[3] Center of Chemistry, Sciences Institute, BUAP, C.P. 72570 Puebla, Mexico

[4] Laboratory of Theoretical Chemistry, Faculty of Chemical Sciences, BUAP, C.P. 72570 Puebla, Mexico

Published online: 21 May 2025

of each domain, resulting in four VSDs (VSD$_{DI}$, VSD$_{DII}$, VSD$_{DIII}$ y VSD$_{DIV}$), which are positioned around the pore domain, which is made up of the S5 and S6 segments of each domain, allowing the formation of 4 pore domains (PD; PD$_{DI}$, PD$_{DII}$, PD$_{DIII}$, PD$_{DIV}$). Within the pore domains, there are relevant amino acids that confer selectivity to the sodium ion; these four amino acids are known as the DEKA selectivity filter. This acronym is due to the fact that it is made up of aspartic acid, glutamic acid, lysine, and alanine [4]. (Fig. 1), while all β subunits (β1 to β4) belong to V-type Ig-like an extracellular, the transmembrane segment, and the intracellular C-terminal [2–8].

The β3 subunit is mainly expressed in the adrenal gland, heart, kidney, and peripheral nervous system. It is thought to be associated with certain health conditions in patients, such as epilepsy or cardiac arrhythmia [6]. Until now, no data has been published on an atomic scale for the contact zone between the α and β3 subunits of subtype hNa$_v$1.7. It was hypothesized that β3 could bind between α domains DII/DIII and DIII/DIV.

Biophysical studies observed for Na$_v$1.5 a possible direct modulation in the DIII-mediated deactivation process [9]. The β3 subunit generates changes in the inactivation of the steady state towards more positive potentials [10] and allows a recovery of the channel from the inactivated state [11]. In addition, it was observed that β3 changed the voltage values necessary for activation towards hyperpolarizing potentials and increases the number of channel pores which remained available in the membrane for pore opening [12], and makes Na$_v$1.7 less susceptible to several blocking agents [11].

The β subunits are transmembrane proteins with an N-terminal extracellular domain. The latter belongs to the all-beta protein superfamily, which does not show helical secondary structures but almost entirely beta sheets (all-beta topology). Their overall fold is homologous to the V-set family of immunoglobulins (Ig), which includes cell adhesion molecules (CAM) [6]. In the extracellular domain, it presents very large handles that are called complementarity determining regions (CDR's); these are responsible for sensing or interacting with the antigen and, in this case, with the sodium channel [13]. They regulate neuronal excitability and constitute druggable biomolecular targets [8, 14].

The PPI site between the subunits α and β1 has already been elucidated for various voltage-gated sodium channels (Nav). PDB entries for Na$_v$1.2: 6J8E [15], for Na$_v$1.3: 7W77 [16], for Na$_v$1.4: 6AGF [17], for Na$_v$1.6: 8FHD [18] and for hNa$_v$1.7: 6J8I [19]. At the beginning of this study, only PDB entries (https://www.rcsb.org/) to the year 2019 were available (see Table S1 [20]). Two PDB entries were released, one before we started (6 J8I [19]) and one mid-way (7 TJ8 [21]) with cryo-electron microscopy (cryo-EM) structures. PDB entry 6J8I shows α/β1 complex of hNa$_v$1.7, but not its α/β3 complex—whereas the other PDB entry 7TJ8 represents an α/β3 complex, but not for the voltage-gated type 1.7 of human sodium channels (hNa$_v$1.7). Until now, the complex between subunits α and β3 has not been determined experimentally for hNa$_v$1.7 [22–46]. Hence, we generated it computationally to study the α/β3 PPI at an atomic scale. We compared our 3D model to both cryo-EM images as references. They complement each other: 6J8I with a correct α but incorrect β, and 7TJ8 with an incorrect α but a correct β3 subunit in the complex structure (see Table S1). Recently, the biochemical electrophysiological modulation of tetrodotoxin (TTX) and conotoxin as binders to Na$_v$ α/β complexes was reported [47–51]. Regulation of genes which express Na$_v$1.7 channels, along with β4, was studied in cancer-related health issues [52, 53]. The α subunit of human Na$_v$1.7 has also been related to peripheral pain signalling toward the brain and associated with certain genetic variations of the human gene SCN9 A. Some of them could change individual pain perception in patients [54–62]. In more extreme cases, after suppression of the channel expression, a complete loss of sensitivity was observed in animal studies [63, 64]. The findings helped develop a new group of drug candidates as so-called "Na$_v$1.7 inhibitors" [65–69].

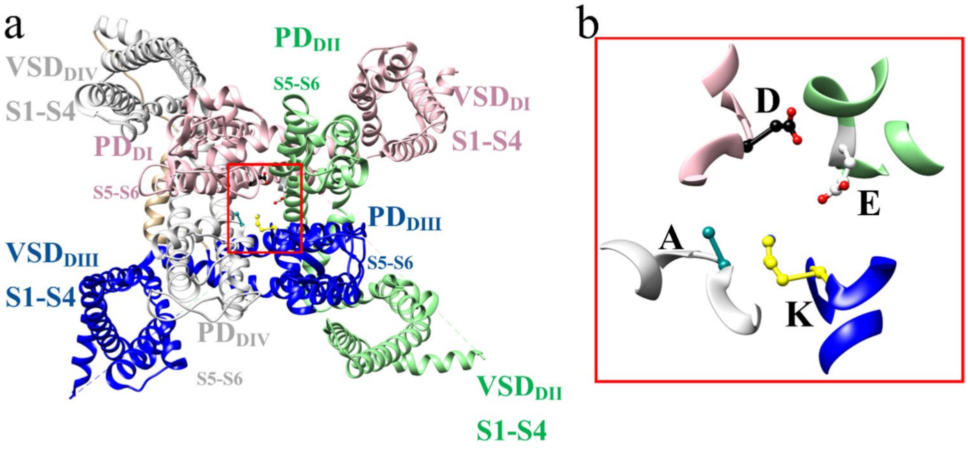

Fig. 1 Three-dimensional topology of the sodium channel, **a** the topology shows the positions of the four voltage-sensing domains (VSDs) and the four pore domains. The color coding is pink for DI domain, light green for DII domain, blue for DIII domain, and gray for DIV domain. **b** The selectivity filter is made up of aspartic acid (black), glutamic acid (light gray), lysine (yellow), and alanine (cyan), lysine being the most crucial for selectivity

Other genetic studies with subunit $\beta3$ found implications for impaired cardiac activities, such as atrial fibrillation [70].

Little information, such as glycosylation patterns, but no structural information has been provided for the $Na_v1.7$ α and $\beta3$ complexes until 2013 [12]. Possible interaction zones between $\beta3$ and α were systematically analyzed for all known sodium channel subtypes by our group, and it was proposed that the subunit $\beta3$ would be in contact with domain DIII [71]. The Ig-like domain interacts with the extracellular portion of the transmembrane segment of S1 and S2 [24]. Earlier, other group members carried out mutational and computational studies on $\beta1$ subunit, trying to identify amino acids at the hitherto unknown $\alpha/\beta1$ interface [72]. They described a loss of channel function by patch-clamp tests for $\beta1$ with a double mutant, which turned out to be a glycosylation site when the crystal structure was elucidated in 2017. Two adjacent hairpin residues, TN, were mutated to AA (dubbed as TANA), which probably hampered posttranslational trafficking to the cell surface (frog oocytes for tests), all of which led to the aforementioned loss. Recently, the binding of β to α central unit was elucidated by cryo-EM (PDB entries: 6J8I and 7JT8). Interestingly, the amino acids at the $Na_v1.7$ and Nax α/β interfaces have remained remarkably conserved, with an 85% identity score, while other parts did not. The DIII domain of both channel types—which is the domain of α/β interaction—has an overall identity percentage of 53%.

For a better understanding of the binding of auxiliary/accessory proteins to voltage-dependent sodium channels, it is necessary to generate experimental models and theoretical structural models that explain the PPI. Identification of those PPI residues is a prerequisite to explain the molecular events of channel modulation. The functions of certain residue segments and binding sites for the $\beta1$ subunit on several of the sodium channel isoforms have been reported. On the other hand, how $\beta2$ and $\beta4$ subunits bind to the sodium channel through an extracellular disulfide bridge in the N-terminal domain has been described, too. Albeit, research concerning $\beta3$ subunit modulation on sodium channels has been reported to a much lesser extent than for $\beta1$. Hence, not only the PPI but also the modulation mechanism had both remained unknown [71–80]. Further evidence comes from published findings on ion channel research with other types than voltage-dependent sodium channels [81]. Despite the sheer number of structural information released until the start of this study in 2019, and beyond, the structure of $Na_v1.7$ complex between α and $\beta3$ subunits has not been experimentally elucidated (Table S2). Hence, in this study, we aimed at generating the model at atomic scale and characterizing the interactions between both subunits to shed light on the computed interface between Na_v α and $\beta3$ subunits. The second purpose was to simulate sodium cation passage through α in the presence and absence of $\beta3$. This could be achieved only for the upper part of the $hNa_v1.7$ pore segment because the model reflects the inactivated state of the underlying template.

Methods

Retrieving and analyzing primary sequences

FASTA search for primary sequences of the subunits and multiple sequence alignments (MSA) were carried out at EMBL-EBI with the web-based tools (https://www.ebi.ac.uk/jdispatcher/sss/fasta and https://www.ebi.ac.uk/jdispatcher/msa/clustalo) [82–85]. General bioinformatic tasks, like MSA or inspection of PDB entries, were carried out by Vega ZZ version 3.2.3 [86].

Modelling the α subunit

The sequence of the α subunit of the sodium channel $hNa_v1.7$ was obtained from UniProt (https://www.uniprot.org/uniprotkb/Q15858/entry). Homology modelling was based on two structures: (i) 7XVF [42] to model the N-terminal domain by homology; (ii) 6J8I [19] to model the transmembrane portion by homology. We used AlphaFold for our incomplete $hNa_v1.7$ model (https://alphafold.ebi.ac.uk/entry/Q15858) to add the missing α helices found in the intracellular segments. Moreover, the spatial coordinates of PDB release 4JPZ were extracted [21] to model the C-terminal domain. Modeller 9.14 was installed as add-on program [87–90] to the Chimera package version 14 [91] to create the final target structure by homology modeling with the aligned UniProt target sequence [92]. The models coming from the different structures were merged under Pymol [93]. The quality of the complete model was verified using the QMEAN value. To this end, its PDB model was uploaded to the Expasy QMEAN database [https://www.expasy.org/resources/qmean] [94, 95]. High quality can be expected with values from 0.6 to 1.0 range. All QMEAN values lay in this range, too, for the transmembrane segments of N- and C-terminal domains (Fig. S2).

Modelling the β3 subunit

The amino acid sequence of the human $\beta3$ subunit was retrieved from UniProt KB under the UniProt code Q9 NY72 (https://www.uniprot.org/uniprotkb/Q9NY72/entry). MSA on β isoforms was carried out using the sequences in Fasta format from the EMBL-EBI website (https://www.ebi.ac.uk/jdispatcher/sss/fasta) under Clustal Omega (https://www.ebi.ac.uk/jdispatcher/msa/clustalo) [82–85]. The resulting primary sequence comparison yielded a closer relatedness by homology between target $\beta3$ to $\beta1$ than $\beta3$ to $\beta2$ or $\beta4$ (Table 2).

Next, the 3D model of the human $\beta3$ subunit was created under Chimera version 14 [91]. The extracellular domain of $\beta3$ could be taken directly from a homo-trimeric crystal structure of $\beta3$ (PDB entry 4L1D [24]). To model the missing transmembrane part only, we searched known PDB entries with a β complex and discarded those with $\beta2$ or $\beta4$ as not suitable 3D templates (PDB entry 6J8I [19]). The transmembrane segment, along with the intracellular C-terminal domain, had to be extracted from another crystal structure of $\beta1$ which had the highest homology (PDB entry 6J8I [19]).

The extracellular (at the N-terminal segment) of $\beta3$ had already the correct amino acid primary sequence. In contrast, the primary sequence of the transmembrane segment had to be changed from $\beta1$ to $\beta3$ using again Modeller 9.14 [87–90] under Chimera version 14 [91]. Extracellular and transmembrane domains were fused under Pymol [93]. After merging 4L1D and 6J8I to generate a complete 3D model of $\beta3$, we verified that no residues were cut out or duplicated. The homology modeling tool of version 9.14 of Modeler was used, which has been integrated in Chimera as add-on [87–91]. This way, our final 3D model was based on the complete primary protein sequence for human $\beta3$ from UniProt KB with UniProt code Q8 NY72 (https://www.uniprot.org/uniprotkb/Q9NY72/entry) [92]. The quality of the $\beta3$ subunit model was assessed as mentioned before for the alpha subunit. The resulting value range was the same (Fig. S2).

Refining the structure of the 3D models

Prior to creating a crystal structure–like complex of the two subunits, each one had to be converted into a refined 3D model because bad contacts (clashes) existed between many side chains. Hence, each model underwent a separate geometry minimization process during 100 ps in the CHARMM36 force field version 2021 (http://mackerell.umaryland.edu/charmm_ff.shtml#gromacs) under GROMACS version 2021.4 [96–98]. Both α and $\beta3$ subunits were placed into larger molecular systems, AKA solvent boxes. Each box contained the respective subunit plus solvent molecules of TIP3P water type with the solved electrolyte NaCl at a concentration of 0.15 M. The system was exposed to a temperature of 310.15 K. Firstly, the system was subjected to NVT and NPT minimizations for 100 ps each.

After minimization, no bad contacts were observed applying Chimera's verification tool (Menu > Tools > Structural Analysis > Find clashes/contacts) [91]. In the same way, the Psi and Phi angles were also compared using Ramachandran tables obtained from the SwissPDBViewer tool [99, 100] (select > all; Wind > Ramachandran Plot). Fig. S3 panel (a) illustrates hNa$_v$1.7 subunit α before minimization, whereas panel (b) displays hNa$_v$1.7 subunit α after structural minimization. In addition, Fig. S4 panel (a) shows subunit $\beta3$ before structural minimization. Panel (b) depicts subunit $\beta3$ after structural minimization. After the CHARMM36 refinement of α and $\beta3$, they both were extracted from their respective TIP3P water box. Both refined and water-free models served as input for docking simulations by HDock [101, 102] and HADDOCK 2.4 [103, 104].

Modelling the α/β3 interface by docking

By means of molecular docking, the unknown PPI between α and $\beta3$ was computationally determined. To this end, we used HDock [101, 102] and HADDOCK software for flexible docking [103, 104]. HDOCK requires the input in PDB format of both proteins. The standard settings were applied. The output complex was retrieved from the Web page [102]. HADDOCK requires both proteins separately as input, with a limited number of up to 150 interface residues. Our model was restrained to 150 contacting residues on each side of our $\alpha/\beta3$ model. The docking result was retrieved from the web server. Back docking was performed on the hitherto known $\alpha/\beta1$ complex of PDB entry 6J8I. Next, blind docking at the unknown $\alpha/\beta3$ interface was carried out. The docking score was transformed into a confidence score to assess the probabilities of complex formation between both proteins. The docking outcome was visualized under Chimera.

Modeling the complete system for molecular dynamics

In the next step, we added more components to the 3D model, as outlined in the following:

(i) A pre-established 1-palmitoyl-2-oleoyl-sn-glycero-3-phosphocholine (POPC) molecule was chosen as a building block for the lipid membrane on the WEB-online platform CHARMM-GUI (https://www.charmm-gui.org/) [105–107]. (ii) An extended membrane model was generated with 1298 POPC. (iii) Next, it was minimized and equilibrated during the preparation step on this Web platform. (iv) Thereafter, our $\alpha/\beta3$ complex (without solvent box) was processed under CHARMM36 force field conditions, allowing the N-terminal and C-terminal to meet their positive (+) and negative (−) charges, respectively. Next, the $\alpha/\beta3$ complex was placed in the middle of the membrane system with the orientation of orientations of proteins membranes (OPM) [108] and solvated with TIP3P water. (v) A salt concentration of 0.15 mM NaCl was added to reflect isotonic physiologic concentrations. To avoid the movement of the protein chains during the minimization processes, a force of 100,000 kJ/mol-nm^2 was added to the heavy atoms. (vi) An energetic minimization of 500,000 steps was performed to allow the system to be at a total force below 1000 kJ/mol nm. The system underwent two successive thermodynamic equilibration simulations: (1) NVT (500,000 steps equal to 1 ns) under a modified Berendsen V-rescale thermostat, with the LINCS constraint algorithm at a temperature of 310.15 K and followed by another non-productive run, namely (2) NPT (1,500,000 steps equivalent to 3 ns) under a Parrinello-Rahman type barostat with a Nose–Hoover type thermostat, cubic interpolation 4 (PME-order), short-range electrostatic cutoff, and short-range van der Waals cutoff to 1.2 nm, Fourier-spacing 0.16, using the same LINCS constraint algorithm at a temperature of 310.15 K. Prior to production runs, this complete system was optimized again to avoid bad contacts and geometric distortions.

Three systems were generated to determine the stability of the system: (i) complete $\alpha/\beta3$ subunit in water; (ii) DIII domain of the α subunit/$\beta3$ subunit in a lipid membrane; and (iii) complete α subunit/$\beta3$ subunit in a lipid membrane (Table 1). Taking a temperature variation of 323 K, generated to ensure that there are no phase changes in the lipid membrane, as Tieleman showed that due to the physiological temperature, in a simulation there can be membrane rupture or a poor recreation of the biological environment [109]. In addition, to show that there is stability in the model since it could become depolymerised in the simulation.

Running the complete system by molecular dynamics

To study the $\alpha/\beta3$ interface, as well as the sodium ion passage, MD production runs had to be applied on a huge system after incorporation of (i) a lipid membrane model, (ii) TIP3P water, as well as (iii) NaCl ions to the target protein complex.

The prepared system was subjected to the leap-frog integrator with 50,000,000 to 1,500,000 000 steps, resulting in MD data for observation time windows between 100 and 300 ns. Finally, the production runs were carried out under GROMACS [97–99], in its 2021.4 version, in a supercomputing center at the "Laboratorio Nacional de Supercomputo del Sureste de Mexico." The generated trajectories were visualized under the VMD program [110] and the graphs were generated with the XMGrace program [111]. To analyze the trajectories of the MD simulation, it is done using commands that are specific to Gromacs 2021.4. To calculate the root-mean-square deviation (RMSD) is used to measure the stability/changes of alpha carbons in both subunits through time [112]. This is done using the command gmx_rms. To generate the root-mean-square fluctuation (RMSF) is done using the command gmx_rmsf, and to analyze the distance of the amino acid, it is done using the script "distance.tcl" specific to VMD, which measures the distances between amino acids from the centre of mass.

Determining the affinity of the Ig-like domain for the sodium channel

From the MD results, affinity calculations were performed with the Linux-based tool APBS (adaptive Poisson-Boltzmann solver) at https://server.poissonboltzmann.org/ to determine the interaction energy and its solvent accessible surface (SAS) (Fig. S1, Fig. S2 and Table S1). To calculate APBS, a file containing the following parameters is needed. These help us to describe the compound or residue by means of an isosurface in which it tries to find the possible contacts it makes. The file must contain: (i) the specification of the periodic boundary conditions to be able to calculate the Poisson-Boltzmann equation (pdie = 2.0); (ii) specify the number of grid points per processor (dime = 161 161 161); (iii) specify the length of the coarse grid (cglen = 261 255 293); (iv) specify the fine mesh domain lengths in a multigrid focusing calculation (fglen = 174 170 193); (v) specify that the nonlinear (full) Poisson-Boltzmann equation should be solved (npbe); (vi) specify the dielectric constant of the solute molecule (pdie = 2.0).

Table 1 Systems performed to assess the interaction between both subunits

System	Temperature (K)
Complete α subunit in water	310.15
Complete α subunit in water	323.00
Complete $\alpha/\beta3$ subunit in water	310.15
Complete $\alpha/\beta3$ subunit in water	323.00
DIII domain of the α subunit/$\beta3$ subunit in a lipid membrane	310.15
DIII domain of the α subunit/$\beta3$ subunit in a lipid membrane	323.00
Complete α subunit in a lipid membrane	310.15
Complete α subunit in a lipid membrane	323.00
Complete α subunit/$\beta3$ subunit in a lipid membrane	310.15
Complete α subunit/$\beta3$ subunit in a lipid membrane	323.00

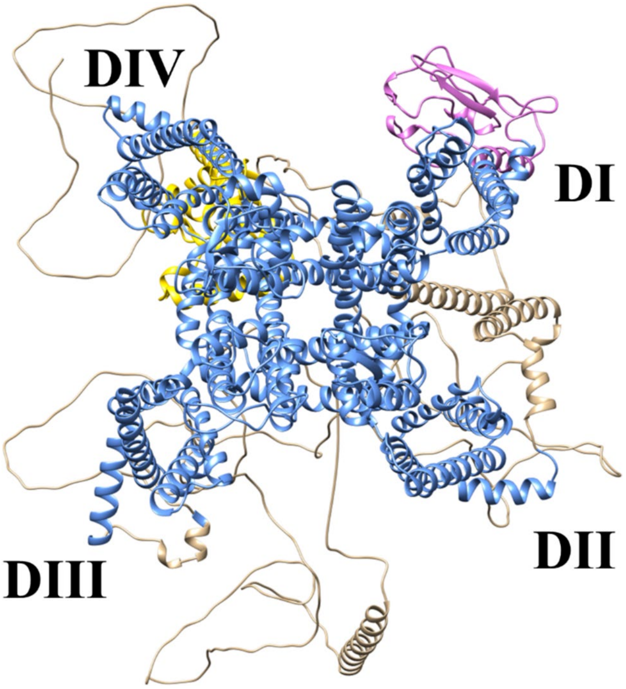

Fig. 2 3D model of hNa$_v$1.7. Color code: orchid for the N-terminal part from template 7XVF; cornflower blue for transmembrane segments from template 6J8I; tan from Alphafold for a missing intracellular loop; gold for the C-terminal part from template 4JPZ

Results and discussion

Three-dimensional model generation

The 3D structure of the extracellular domain of human β3 was extracted from PDB entry 4LID (Table S1). To generate the complete 3D model of the β3 subunit, we fused the structural information for the transmembrane and intracellular domains from 6J8I, which constitutes β1 of hNa$_v$1.7 (Table S2). To generate the complete α subunit model of hNa$_v$1.7, three homologous 3D templates were used: (i) 7XVF for the N-terminal part; (ii) 6J8I for the transmembrane main section with the extracellular loops. Precalculated models of intracellular loops were retrieved from the Web-based server Alphafold (https://alphafold.ebi.ac.uk/) [113]; (iii) 4JPZ for the missing C-terminal domain in the incomplete 3D template 6J8I (Fig. 2). Like 7XVF and 6J8I, 4JPZ also constitutes a closely related 3D template with 70% residue identity. For more details concerning the 3D model generation, see the Supplementary Materials (SM) with the corresponding Fig. S3 to Fig. S7.

Subunit arrangement analysis

Since the VSDs of the channel form a heterotetrameric monocadenar subunit (α), it is not far-fetched to assume the segments S1 to S4 of each could be those in contact with β3. Structural information had been deposited at PDB prior to the start of this work with 5XSY (α/β1 for eel, 2017) and 6J8I (β1/α/β2, for human, 2019). This implies that associations of β2, β3, or β4 were not available during this study. While the location of β1 and β2 was elucidated by cryo-EM, the location of β3 could theoretically replace β1 or β2 (Fig. 3). Also in good keeping, the hitherto known literature has attested that DII and DIII or DIV were the most probably β3 contact partners [10, 12].

Docking analysis at the protein–protein interface

Since the available PDB structures did not represent our specific α/β3 complex but rather complexes with other types of β subunits, we carried out docking simulations with random start positions by HDock [101, 102] and HADDOCK2.4 [103, 104] (Fig. 4). For more details concerning the docking

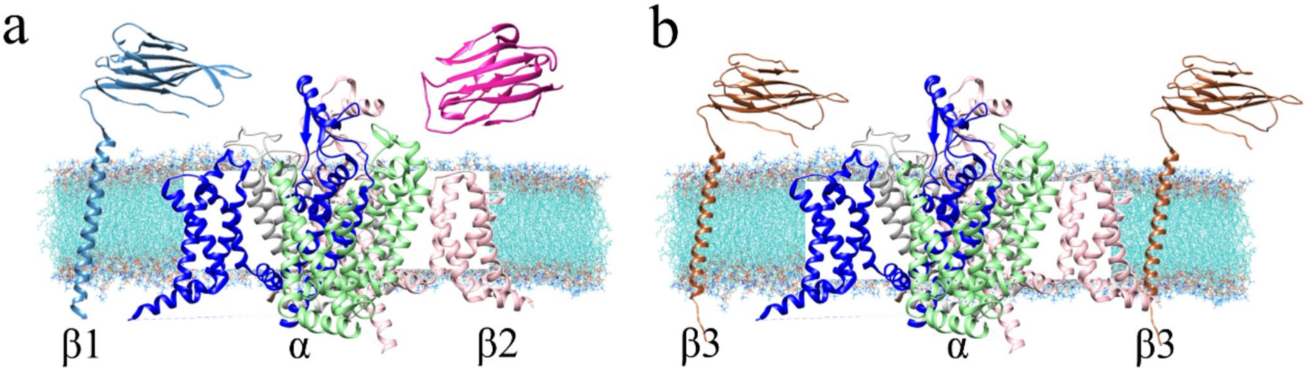

Fig. 3 Topology of subunits on hNa$_v$1.7. **a** Structurally known β1/α/β2 complex. **b** Two possible arrangements for β3 for hitherto unknown α/β3 complex. The diagonal line symbolizes the PPI. Color code: β1 subunit cyan, β2 magenta; sodium channel: DI domain pink; DII light green; DIII blue; DIV light gray; and β3 subunit sienna, and a lipid membrane in blue with red dots

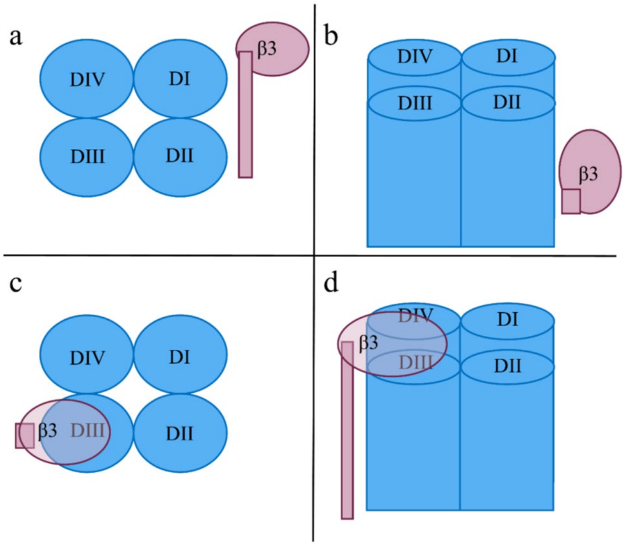

Fig. 4 Random start position in panels **a** and **b** and the final docked pose in panels **c** and **d**. Panels **a** and **c** are top-down views, while panels **b** and **d** are lateral views. Color code: pink *β*3 and blue *α* subunits with four domains D1 through DIV

Table 2 Identity score percentage for *β*1, *β*2, and *β*3

	Eel *β*1 [PDB code 5XSY]	**Human *β*1 [PDB code 6 J8I]**	**Human *β*2 [PDB code 6 J8I]**	**Human *β*3 [PDB code 7 TJ8]**
Eel *β*1	100	46	20	42
h*β*1	46	100	21	50
h*β*2	20	21	100	23
h*β*3	42	50	23	100

results between the *α* and *β*3 subunits, see SM with the corresponding Fig. S8 to Fig. S14.

The homology of the three types of *β* subunits was also assessed at this stage of work (Table 2).

To study the *α*/*β*3 interface, we needed a 3D model of the *α*/*β*3 complex. We chose random start positions for the *β*3 as a sort of "ligand" for the α subunit "receptor" with its huge molecular size. The docking results were inspected, and the docked poses were found only slightly different from the reference structures *α*/*β*1 (PDB code 6 J8I) or *α*/*β*2 (PDB code 6 J8I) [19]. Figure 5 shows the PPI model with two extracellular loops between transmembrane segments S1 and S2, as well as S3 and S4 on domain DIII of the *α* subunit in complex with *β*3. As a proof of concept, the *β*1 ligand in the *α*/*β*1 complex was successfully self-docked to its position in the reference complex (PDB entry 6 J8I [19]). Almost at the end of this study, with the advent of an experimentally determined *α*/*β*3 complex, the computed model with domain DIII as the interaction site could be validated (PDB entry 7 TJ8 [21]). For details about the computed results and determination of the protein–protein complex by MD, see Fig. S15 through Fig. S40 in SM.

Stability analysis for molecular dynamics model

The hitherto unknown PPI between both subunits (*α*/*β*3) of hNa$_v$1.7 were studied at an atomic scale by MD [114]. The 3D model, which the simulation was generated, is made up of (i) *α* subunit; (ii) *β*3 subunit; (iii) lipid membrane of POPC; (iv) NaCl 0.15 M; and (v) water tip3p at 310.15 K. This complex model stability under MD conditions between both subunits is remarkable since there was no 3D template available at the time of the study for 3D model generation. Root mean square deviation analysis of atom distances (RMSD) showed that the model system remained stable during the production run of 300 ns and beyond (Fig. 6). RMSD averages the distance measurements of initial atom positions to their respective positions at a given moment in time during MD production runs. Values ranging from 3 or 4 to 6 or 7 could reflect larger displacements in space, e.g., domain shifts, structural deformations, or overall model instabilities [115]. Global RMSD studies include geometrical changes in irrelevant molecule parts, but RMSD for selected atoms focuses on spatial movements of interest [116].

This finding also reflected that our system was successfully prepared by minimization with NVT followed by NPT prior to MD production runs. Of note, the rising RMSD values in the first 10 ns did not reflect structural instability, but rather indicated rearrangement in the extra- and intracellular loops (a in Fig. 6). On the other hand, the *β*3 subunit behaves similarly due to its intracellular loop which underwent rearrangements during the first 10 ns. Thereupon, minor fluctuations in the RMSD ceiling line can be detected, which stem from the highly mobile complementarity determining regions CDR1, CDR2, and CDR3 of the extracellular domain on *β*3 (b in Fig. 6). Typically, they possess antigenic functions in Ig proteins [117]. The fact that the amino acids on both proteins have really "seen" (contacted/interacted with) each other during eons of evolutionary time led to a successful combination of docking and MD simulations with the computed identification of the *α*/*β*3 interface. Otherwise, missing neighborhood effects would have led to molecular models with more repulsion than attraction forces.

To explore the overall stability of the 3D model with hNa$_v$1.7, the MD observation time was extended to 300 ns. In Fig. 7, the data was filtered to focus on the domain DIII. The RMSD values remained constant in a range of approximately 0.1 nm, which represents a typical value for overall protein stability. RMSD values were based on the alpha-carbon atoms of the DIII amino acids. The protein stability was deduced—despite the steady increment of the absolute

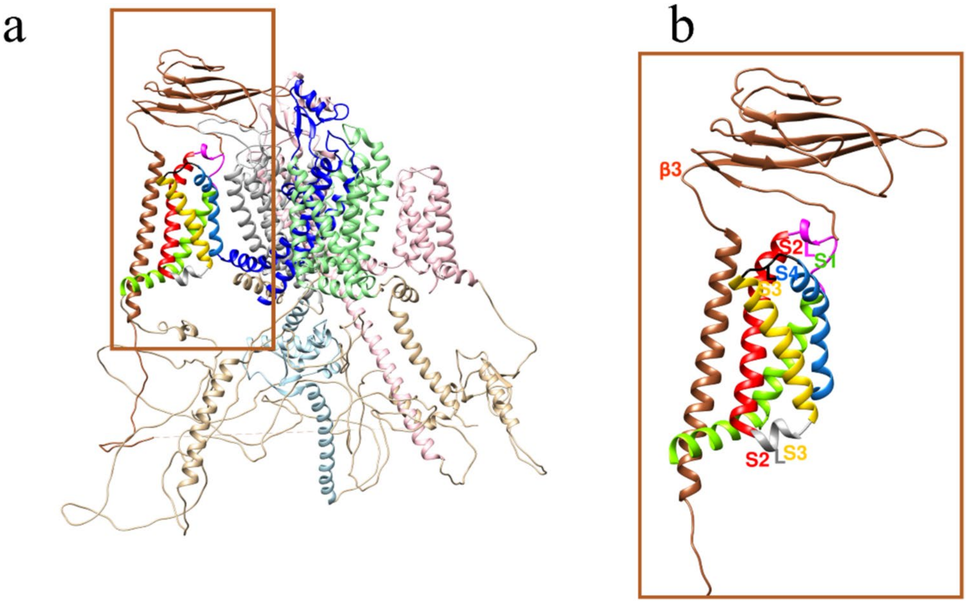

Fig. 5 3D model of the docked $\alpha/\beta3$ interface. The $\alpha/\beta3$ interface is located on the DIII domain of the subunit α. Only the mechanistically relevant DIII segments are displayed. Two extracellular loops at the $\alpha/\beta3$ interface are labelled with their transmembrane segments (S1-L-S2 and S3-L-S4). The extracellular Ig-like domain of $\beta3$ contacts both loops. Between both loops lies another loop facing the intracellular side between S2 and S3 (gray ribbon). The C-terminal part of $\beta3$ also orients toward the inside (C-ter). Color code for protein backbone ribbons: $\beta3$ model in sienna; S1, S2, S3, and S4 of α subunit in chartreuse, red, yellow, and cornflower blue colors; DI, DII, DIII, and DIV in pink, light green, blue, and light gray, respectively. Colors for two loops at the PPI: the first between S1 and S2 in magenta; and the second between S3 and S4 in green

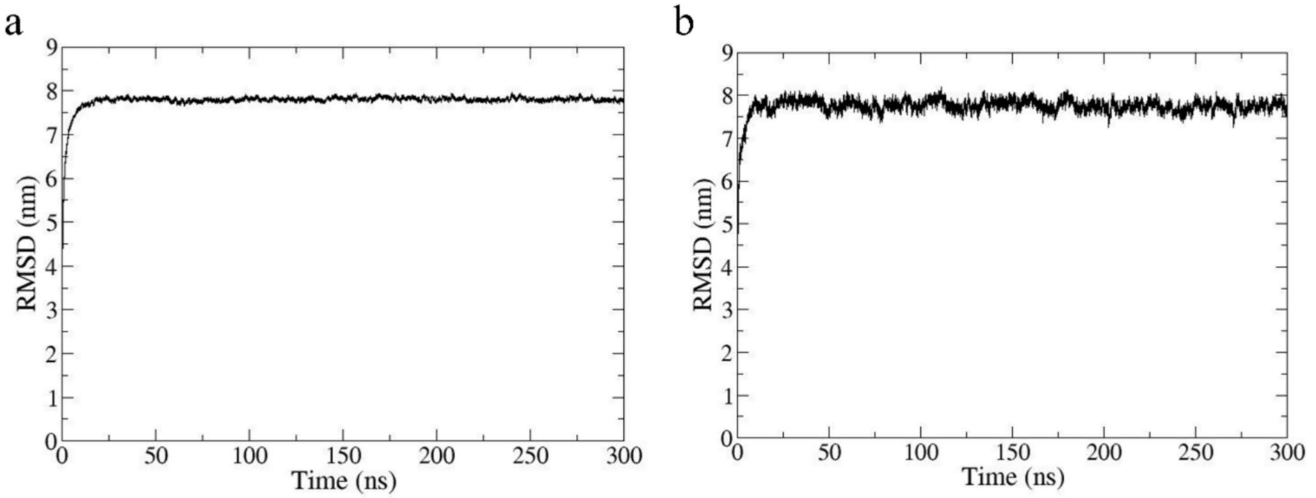

Fig. 6 RMSD plots of the α-subunit and $\beta3$-subunit of the hNa$_v$1.7 sodium channel over 300 ns. **a** RMSD plot of the α-subunit is presented, and **b** RMSD plot of the $\beta3$-subunit is presented

RMSD values—because the values oscillated around 0.1 to 0.2 nm (RMSD fluctuation).

Even the longest MD test run with 300 ns proved that the interface was stable without indications of unfolding the tertiary or secondary structures. During eons of evolution, the interaction between both has been adapted and optimized. Such neighboring effects concern the residues in the voltage sensing domain (VSD) of DIII (VSD$_{DIII}$) [116, 117]. Switching from structural to functional aspects of MD, this phenomenon of side chain proximities between corresponding counter amino acids on both subunits reflects a channel modulation process engaging with DIII of the α subunit of

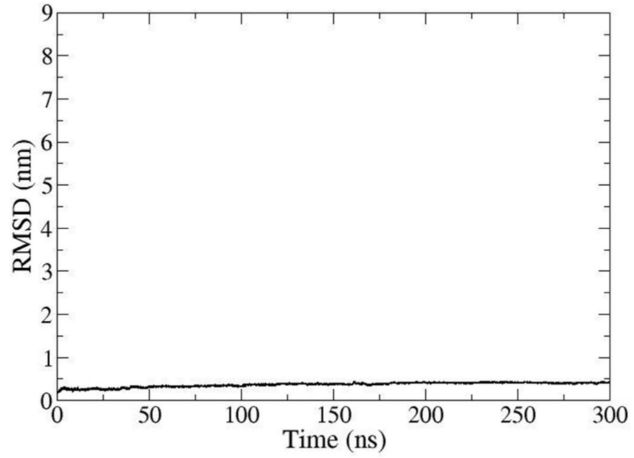

Fig. 7 RMSD plot of VSD$_{\mathrm{DIII}}$. The MD run lasted 300 ns for a larger observation time window. The RMSD values on the graph were registered for atoms of S4 in movement

hNa$_v$1.7. The complex remains stable since the RMSD for DIII oscillates very little during 300 ns of the large observation time window (Fig. 6 and Fig. 7).

We observed S4 mobility in the VSD$_{\mathrm{DIII}}$ of the DIII domain. Figure 8 shows details for the participation of two residue pairs K1287 (on α) with F23 (on β3) as well as R1290 (on α) with F23 (on β3). At the beginning of the simulation, if the interaction between F23 and K1287 is carried out by cation-π, and with arginine, they are only long-range electrostatics, since, as Infield (2021) and Gallivan (1999) mention, the interaction must be well oriented and with a distance of 6 Å [118, 119]. Both cationic residues belong to the VSD. Table 3 lists the positive charges from all the side chains of Arg or Lys for DI through DIV.

As a proof of concept for not only the neighboring effects but also to which degree our MD reflects natural behavior can be extracted from root mean square fluctuation (RMSF)

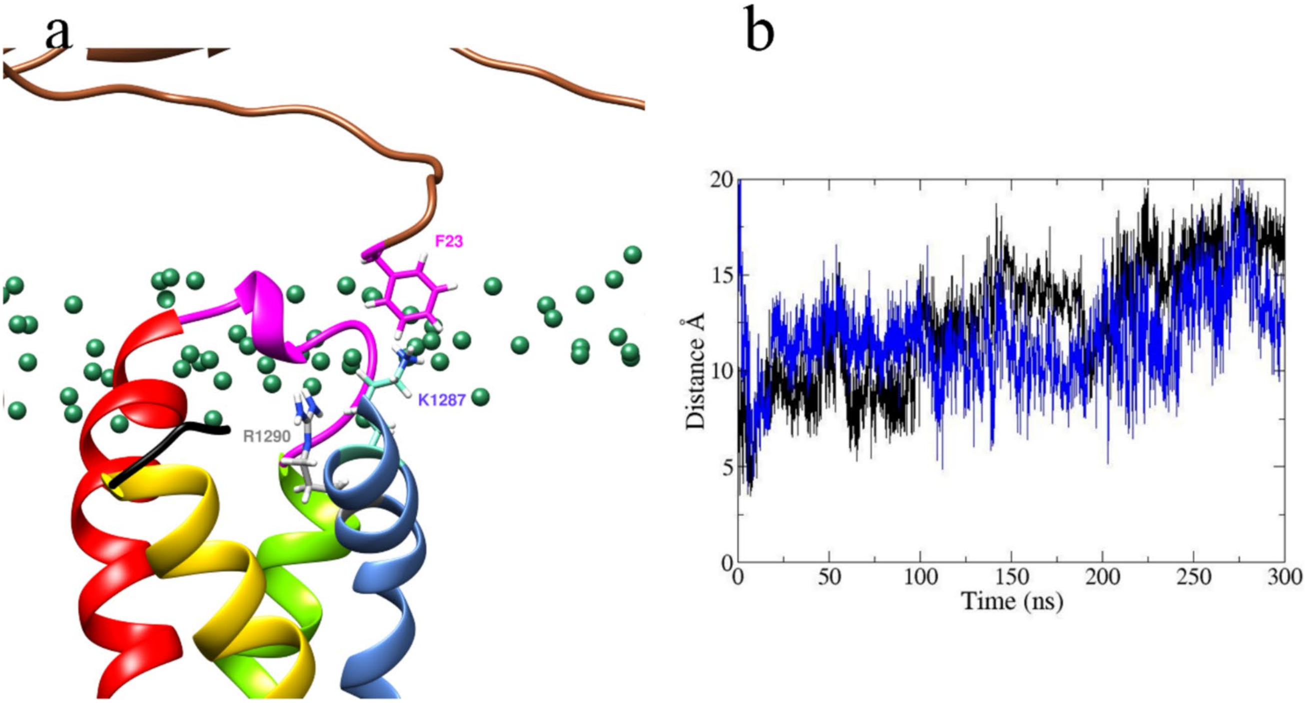

Fig. 8 Representation of the interaction between F23–K1287 and F23–R1290. Panel **a** Interaction between F23 (fuchsia) to K1287 (aquamarine blue) and F23 (fuchsia) to R1290 (gray) which is reflected by the steeply descending slope and the upwards movement at 10 ns. Figure was made with Chimera. Panel. Color code for protein backbone ribbons: β3 model in sienna; S1, S2, S3, and S4 of α subunit in chartreuse, red, yellow, and cornflower blue colors; the green sphere is the phosphate group of lipid membrane. **b** Plot of the distance in the formation of a cation-π interaction between F23–K1287 (black) and F23–R1290 (blue) during the 300 ns

Table 3 Listing of the positive charges of arginine and lysine side chains at the VSD [93]

Domain	Total positive charge	Top-down order of Arg and Lys residues with id numbers
DI	4	R214, R217, R220, K223
DII	5	R835, R838, R841, K844, K847
DIII	6	K1287, R1290, R1293, R1296, R1299, R1303
DIV	5	R1610, R1613, R1616, R1619, R1622

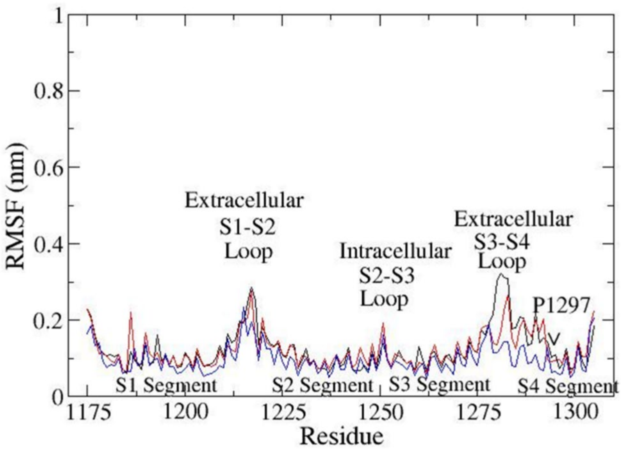

Fig. 9 RMSF plot for VSD_{DIII} of the α subunit over the 300 ns of registered productive run time. The high mobility of the amino acid residues shows the elevation on the RMS: the first peak is formed with amino acids from S1 to S2 extracellular loop. The latter embraced amino acids 1212 to 1224. The second peak was composed of amino acids from the S2 to S3 intracellular loop with residues 1244 to 1257. The residues 1277 to 1284 belong to the extracellular loop between S3 and S4, while the first amino acids of the S4 segment were identified as residues 1287 to 1297. The lines show the movement of the structures through the 300 ns; black line = 0–100 ns, red line = 100–200 ns, blue line = 200–300 ns

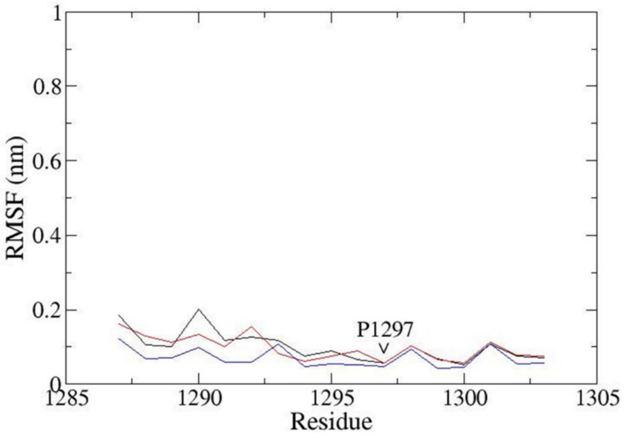

Fig. 10 Representation of the RMSF of the S4 segment of the α subunit. The proline amino acid residue 1297 (P1297) generates a restriction process, making the proline 1297 have greater freedom of movement than before. The lines show the movement of the structures through the 300 ns; black line = 0–100 ns, red line = 100–200 ns. Blue line = 200–300 ns

charts (Fig. 9). Proline P1297 is situated in a helical segment and produces a so-called proline kink (see P1297 between sequence position 1250 and 1300 on the *X*-axis in Fig. 9 and Fig. 10 [120–127]). The total 300 ns observation time was divided by 3. The resulting three 100 ns observation windows in superposition (Fig. 9) revealed an almost periodical repetition of particle mobility, all of which also demonstrates the structural stability—a prerequisite to preserve biological function here of the α subunit. The movement of the other VSD of the channel has a high movement because they do not have a protein that helps them slow down their movement, compared to VSD_{DIII}.

Details about proline P1297 movement can be drawn from the MD playback (Fig. 10). On the RMSF chart (Fig. 10) a more mobile helical region can be identified to the left of P1297, while the residues to the right of P1297 are located in a stiffer helical wheel. Of utmost essence to the mechanistic interpretation of MD, here lies in the fact that this finding nicely explains for VSD_{DIII} how the adjacent arginine residues (R1290 and R1293) move upwards into the extracellular space. And with it, an essential interaction will take place with subunit $\beta3$ and in direct consequence, the channel activation [126, 127].

The S4 segment undergoes a classic "cork-pulling" movement [119]. Proline P1297 of DIII generates a so-called proline kink in the α-helix [119–127] For this reason, The S4 segment consists of two parts: (i) flexible extracellular and (ii) more rigid. It lends larger backbone mobility for most of the extracellular part of S4, whereas, for the inward helical part in the direction of the C terminus, this residue creates a stiffer structure (see also Fig. 9).

The side chain movements of mechanistically pivotal residues were analyzed over time to verify if our MD study correctly reproduces the extant literature (Fig. 11). The book chapter about "The Voltage Sensor Module in Sodium Channels" by James R. Groome and the publication by Sula and coworkers describe the changes that the segment S4 undergoes during channel passage of sodium cations, as well as the different channel geometries. Certain structures show an inactivated channel, while others represent channel geometries that lead to pore opening prior to activation [126–128]. Initially, the side chain of one of them (R1290, orange) was oriented towards E1212 (tan, according to panel (a) of Fig. 11) and R1290 is interacting face to F23 of $\beta3$ subunit; this allows the distance to increase across time. E1212 and R1290, at times it spontaneously formed and opened salt bridges as they quickly increased the separation distance, causing us to go from a strong electrostatic interaction to a weak one over 50 ns. In a timely coordinated or "synchronized" movement, the other arginine (R1293, with blue color in Fig. 11) reoriented, too. It is located deeper inside the channel, right below R1290. Intriguingly, E1212 was "sandwiched" between both (R1290 and R1293). This close contact does not last. Apparently, it is not a stable constellation in space since it does not obey the electroneutrality with anionic residues (*E*) squeezed in between two cationic residues (*R*). The positive total charge excess (+ 1) assists the outward bending on the extracellular end of the helical segment with E1212. This positive charge excess is a

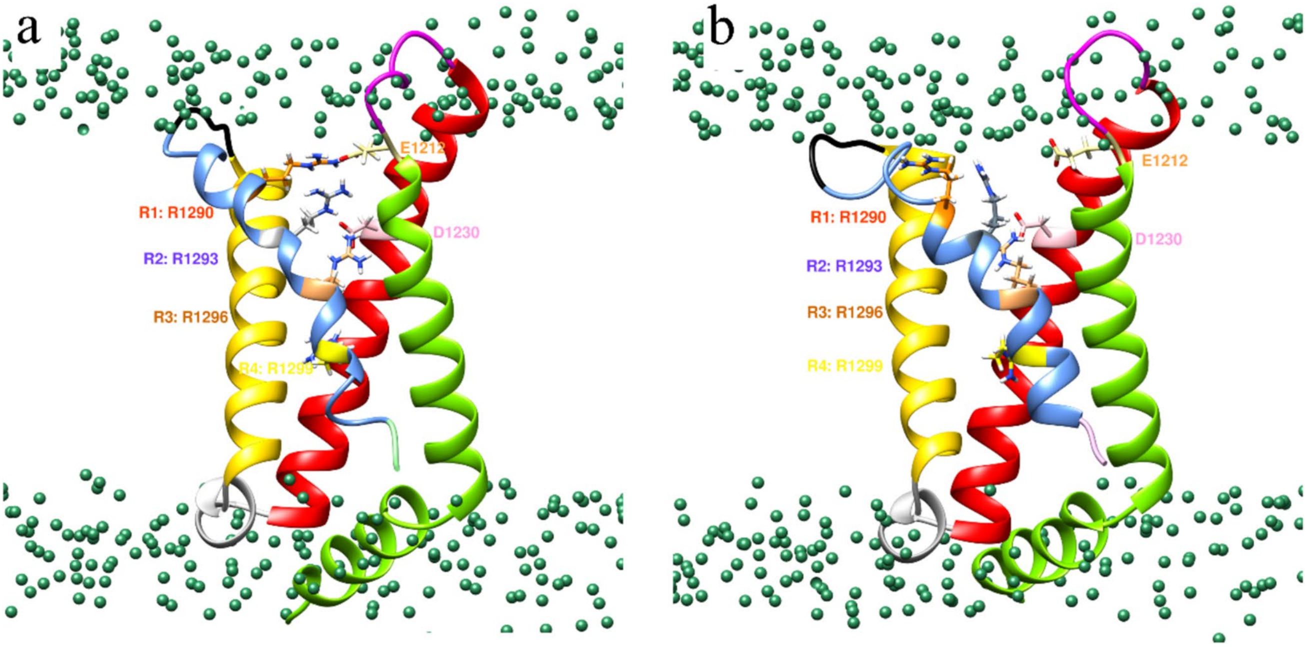

Fig. 11 Structural representations of the conformation change of the S4 of the sodium channel, viewed from inside the sodium channel. Panels **a** and **b** are two models taken from the initial and final time windows (10 ns and 80 ns, respectively). S4 is shown in silver. Panel **a** Inactivated state: R1290 (orange) is oriented towards E1212 (tan) and forms electrostatic interactions; R1293 (gray) is placed below R1290 and interacts with E1212 (tan). They interact with D1230 and R1299 (gold) in the direction of segment S2. Panel **b** Activated state: R1290 (orange) has moved in 70 ns towards the extracellular part. E1212 (tan) interacts with R1293 (gray) as well as R1296 (sandy brown) in the same side chain conformation as R1293. Color code for protein backbone ribbons: $\beta3$ model in sienna; S1, S2, S3, and S4 of α subunit in chartreuse, red, yellow, and cornflower blue colors; the green sphere is the phosphate group of the lipid membrane

well-recognized electrophysiological feature of voltage-gated sodium channels at all four S4 segments—albeit each of them carries a distinct number of arginine and lysine residues. In the context of channel function, this fact also hints at the common characteristics for vertebrate animals, all of which have a heterotetrameric topology based on one primary sequence chain. Whereas the upper part exposed to the channel surface shows the aforementioned mechanistic feature, the architecture of the inner part remains unchanged over time for a twofold reason: (i) it is deeply buried into the membrane bilayer, which holds a firm grip on the transmembrane channel segment; (ii) an adjacent third arginine (R1296) to the two others (R1290, R1293) stays constantly in close contact with D1230. During the entire observation time, this salt bridge was never disrupted. It plays a key role in stabilizing the secondary and tertiary structural elements of S4 on DIII only. The other three domains (DI, DII, and DIV) bear 2, 3, or 5 arginine or lysine residues forming a variable number of non-permanent salt bridges to expose positively charged side chains on the channel surface in a similar mechanistic way as described here for DIII [129]. The pattern is assumed to be recurrent, although the observation time of 100 ns was extended to 300 ns, which was still too short a time frame to observe any periodicity (Fig. S27 through Fig. S40 in SM).

Upon comparison of the MD simulation with $\beta3$ against the other one without $\beta3$ under the same conditions, the electrophysiological role of β3 became evident (Fig. 12 and Fig. 13). In 2013, Leadermann et al. showed that the $\beta3$ presence allows an increase in current density [12] that translates into an increase in the rate at which sodium ions can approach the DEKA selectivity filter. In the MD simulation, it can be observed how the Na ion approaches the selectivity filter more quickly because the $\beta3$ subunit interacts with extracellular loops, preventing the path towards the selectivity filter from being disturbed. In this way, it is known that the sodium ion takes about 30 ns to interact with the lysine of DEKA and to finally be able to pass inside the channel. On the contrary, when the channel is simulated without the $\beta3$ subunit, the Na ion takes about 20 ns to approach the selectivity filter, but the sodium ion can still pass after 50 ns. Once the sodium cation reached DEKA and enters the inner vestibule, both models show highly similar behavior measured as RMSD of Na + against the four residues of DEKA. In Fig. 11, this finding is graphically documented: on the x-axis is the timeline in nanoseconds.

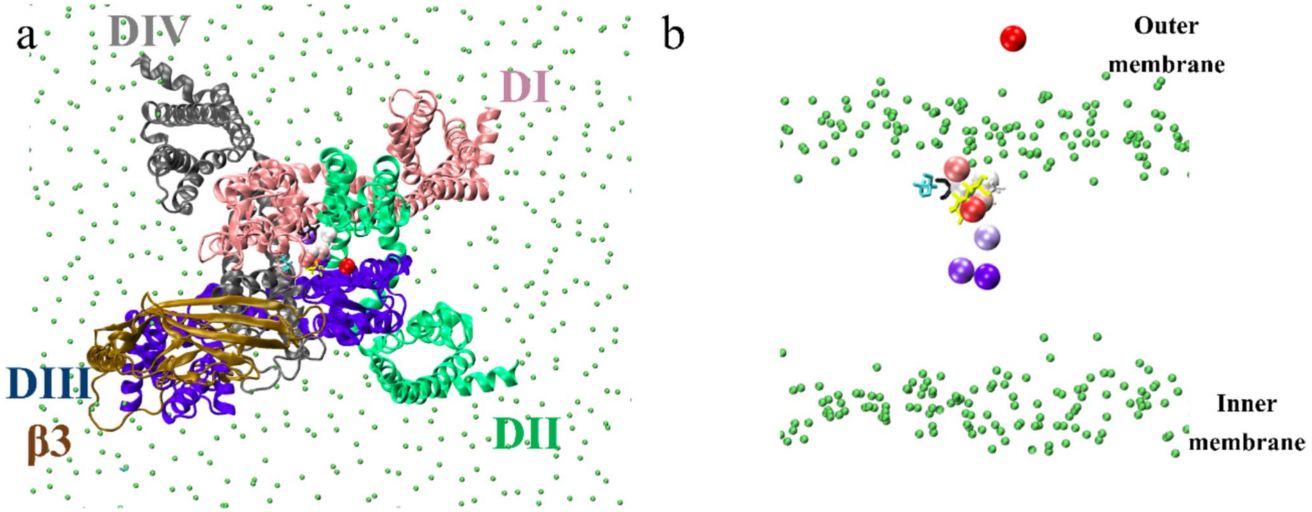

Fig. 12 Display of the Na^{+} trajectory for hNa$_{V}$1.7. **a** Seven sodium locations in the pore are displayed in the $\alpha/\beta3$ complex; the movement of de Na shows the movement and approach to the selectivity filter. **b** Shows only the movement of Na +to the selectivity filter and the position when the sodium passes through across the DEKA ring; the colors of the sodium position through the dynamics range from color red at 0 ns to the passing the selectivity filter, which are light blue to dark blue. The uppermost right location is the starting point at 30 Å distance to the DEKA ring or "bottle neck" (stick model colors: D black, E gaey, K yellow, and A cyan, the green spheres are the phosphate group of POPC membrane). Of note, a deeper permeation of the sodium particle was not possible due to limited supercomputing resources at hand

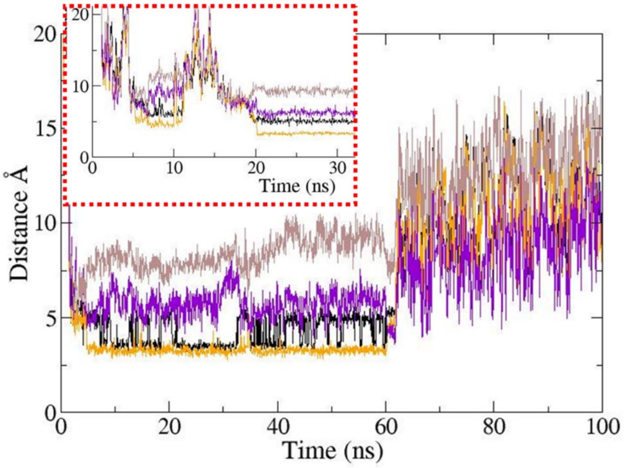

Fig. 13 Distance plot between a passing sodium cation and the four residues of the DEKA-selectivity filter of the α-subunit from hNa$_{V}$1.7. The figure (inlay) shows the Na^{+} behavior, red lines in the absence (respectively absence) of $\beta3$, and the bigger chart is in the presence of $\beta3$ subunit. The observation time on the x-axis for the incoming sodium ion was 100 ns; the starting distance on the y-axis above the outer pore vestibule was 30 Å, and finally, the Na ion passes through because the amino acid lysine of the DIII domain accommodates, showing an increase in distance at 30 ns. A Line colors: black Na +to D; orange Na^{+} to E; purple Na^{+} to K; brown Na^{+} to A

During the first 5 ns, the Na +particle enters the channel pore from the extracellular space. The distance values for the four DEKA residues swiftly decreased while the sodium cation approached them. The chart integrates its movements with respect to each of them as reference locations by super-positioning four lines displayed in four different colors. Two totally different electrophysiological behaviors can occur: one in the presence and the other in the absence of $\beta3$. To visualize these differences, an inlay was created for Na +ions. The seemingly erratic movement was reflected by the fluctuating RMSD values on the y-axis (cf. peaks and valleys in the inlay which is contoured by red intermittent lines). In stark contrast, when $\beta3$ was present in the channel complex model, the incoming sodium cation moved on to the DEKA "bottle neck" without deviation in a rather straight line. The shorter path also saved time, i.e., the sodium passage was faster. This observation is in good keeping with what has been found in electrophysiological studies (patch or voltage clamp experiments) [12]. After passing the DEKA filter step, the cation reached the inner vestibule (Fig. 12). The respective RMSD values on both models were very similar. It is safe to assert that at that stage of the sodium passage there is no significant influence anymore concerning the presence or absence of $\beta3$. This channel segment is too deeply buried in the membrane. Conversely, our observations by MD simulations document that $\beta3$ has an impact upon sodium income only at the channel entrance. For details about the computed results and determination of protein–protein complex by MD studies, Fig. S15 through Fig. S40 in SM.

Neighborhood-related interactions

MD and docking results were analyzed to identify pairs of *α*/*β*3 interacting amino acids on the extracellular PPI such as K1670/E53, E1672/R51, R1218/E28, H1721/P24, and K1287/F23 (Fig. S12 through Fig. S40 in SM). To be precise, the following three *β*3 residues help modulate the function of the *α* subunit: E53 (*β*3) with K1670 (*α*), E52 (*β*3) with K1670 (*α*) as well as R51 (*β*3) with E1672 (*α*). They stay interactive over the entire observation time, which allows modulation with respect to the EDDE filter (aka EEDD). Their distances range between 4 and 10 Å. In addition, the *α*/*β*3 pair K1220/E32 allows for the positioning of the Ig-like segment on the VSDs of the hNa$_v$1.7 sodium channel.

Other *α*/*β*3 pairs do not interact permanently but are in close range and help stabilize the contact zone close to the membrane: K1176/E188; H1191/E176; Y1228/E159; F1194/W172; F1197/W172 (Fig. S11 through Fig. S37 in SM). For instance, a hydrogen bond spans temporarily between the pair Y1228/E159, but at any moment it is lost due to the movement of the membrane chains because the side chain of Y1228 is displaced and reoriented towards the lipid membrane. Hydrophobic attraction could also be observed with F1194/W172 or F1197/W172. With water moieties at a distance, their side chains form a water exclusion (hydrophobic) pocket of variable size according to the overall side chain and backbone movements. Intriguingly, F1197 and W172 rotate to enter stabilizing contact with the membrane lipids. Both cases are only a "pars pro toto" view of the vast concert of hydrogen bond networking for the entire complex, just to name a hydrogen bond residue pair H1191/E176 or a salt bridge between K1176 and E188 in the intracellular segment. For more details, see Fig. S12 through Fig. S40 in SM.

Assumptions and model limitations

In more general terms, our entire simulation study is in excellent keeping with gathered experimental knowledge concerning the complex topology between *α* subunit *β*3, the exact location of the *α*/*β*3 interface at atomic scale, and the spatial rearrangements of interacting loops and pore segments on the subunits, along with sodium particle mobility from the outside to the inner vestibule (Fig. 12). Yet, the model was not amenable to reproducing the complete Na$^+$ passage from the outside to the inside because the model is in the inactivated state and so there cannot be a sodium ion passage, which would require the open state of the channel. The use of the channel in the inactivated state allows us to observe structural changes on the *α* subunit by *β*3 subunit during the inactivated state. To determine the protein/protein stability, we carried out MD studies without membrane but with boxed water for 100 ns. In the same way, another MD run with a 5-degree tilt in the *β*3 subunit was performed. Here, the *α*/*β*3 contact was entirely lost, which represents a significant change in cooperativity between them. In other words, the Ig-like extracellular domain of *β*3 moves, and its new position lies closer to the membrane after 35 ns. A search was carried out for several docking programs, so when using it, and not having the expertise to work with it, a result came up that was very similar to that of HDOCK and HADDOCK, but when performing the dynamics, the extracellular domain binds to the membrane and stays there.

Discussion

With the advent of PDB entry 7TJ8 in 2022, it was possible to validate our predicted *α*/*β*3 interface because, for the first time, an *α*/*β*3 complex was elucidated by cryo-EM techniques [20]. Its chain labeled A constitutes a subunit *α*; yet, it does not constitute our target hNa$_v$1.7 but a hitherto unknown class of voltage-independent sodium channel, called NaX or Na$_x$. Its chain B, however, presents the entire subunit *β*3 of our target voltage-gated sodium channel with its extracellular and transmembrane domains.

In 2019, the PDB entry 6J8I was retrieved as a 3D template at an atomic scale, although it was still not a perfect match because it is a complex with *β*1 and not all identical with *β*3, under study here, namely the human voltage-gated sodium channel hNa$_v$1.7 with its PPI between subunit *α* and *β*3. So, we continued to finish our PPI model until 2024.

As a direct result, the reference confirmed our computed *α*/*β*3 complex with the same orientation and PPI between *β*3 and DIII of subunit *α* (Fig. 14 and Fig. 15). In a final step, the structural data was compared between the reference and the target (Table 4).

The *β*3 subunit interacts with the S4 segment of the VSD$_{\mathrm{DIII}}$. The non-covalent binding in the transmembrane zone was mostly hydrophobic in nature, while those forces that stabilized the binding site of the *β*3 subunit with respect to the *α* subunit were a concert of electrostatic attractions and hydrogen bond networks.

Intriguingly, Glass and collaborators ascribed a PPI stabilizing effect to residue E176 in 2020 (Fig. S22 and S23) [25]. This residue is toward the inner side of the membrane. At the binding site, the interaction is mainly due to hydrogen bonds in addition to electrostatic attractions, as described by Vascon et al. also in 2020 [128]; this interaction prevents the movement of the inner transmembrane helix.

Also, we observed S4 mobility in the VSD$_{\mathrm{DIII}}$ domain with the participation of two residue pairs K1287 (on *α*) with F23 (on *β*3) as well as R1290 (on *α*) with F23 (on *β*3). These interactions show that the S4 segment has two parts: (i) a flexible one after P1297 and ii) a rigid one before P1297. This S4 mobility reflects the observation by Sokolov et al.

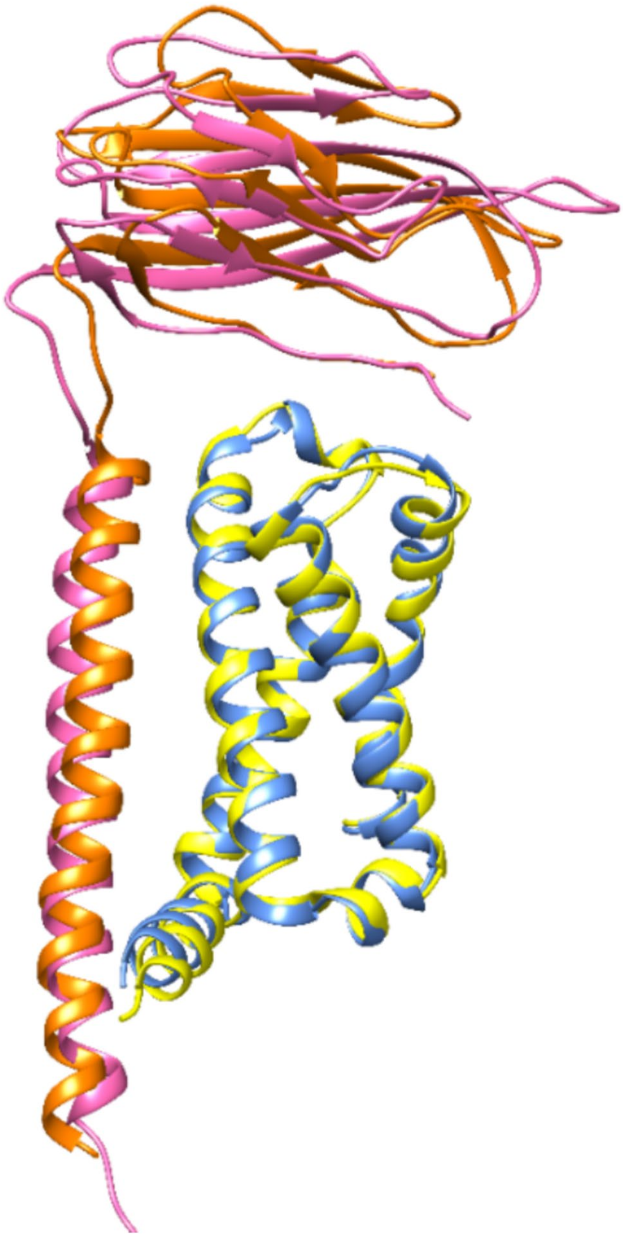

Fig. 14 Experimentally observed structure ($\alpha/\beta3$ of hNa$_x$) and predicted $\alpha/\beta3$ model in superposition. Color code for protein backbone ribbons: blue α model; pink $\beta3$ model; α of 7TJ8 red orange and $\beta3$ of 7TJ8 gold. The $\alpha/\beta3$ interface is located at the DIII domain

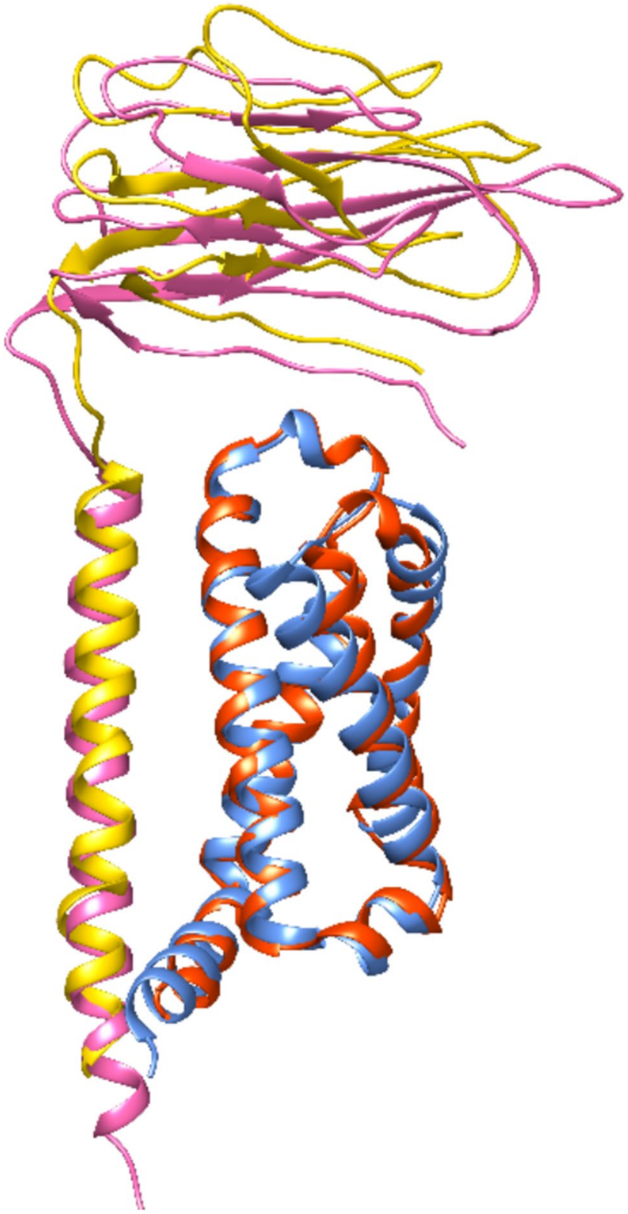

Fig. 15 Experimentally observed structure and predicted model in superposition. The 3D alignment reveals that model $\beta3$ and $\beta1$ from PDB show large geometrical differences due to their different primary sequences. The α subunit of the predicted 3D model, however, fits much better than the $\beta3$ to the cryo-EM $\alpha/\beta1$ complex of hNa$_v$1.7 (PDB entry 6J8I) because both α subunits are the same. Actually, the cryo-EM α subunit was extracted to create the model α subunit. Color code: light blue α model; pink $\beta3$ model; α or $\beta1$ of PDB entry 6J8I = yellow or orange colors, respectively. The $\alpha/\beta3$ interface is located at the DIII domain

in 2018 that the $\beta3$ subunit allows faster recovery from the inactivated state [11]. The interaction between K1287 α/F23, R1290 α/F23, and with the CDRs K1670 at α/E52 at β3; K1670 at α/E53 at $\beta3$; E1672 at α/R51 at $\beta3$; and W1354 at α/E129 at $\beta3$ describes at the molecular level the finding of the modulation process concerning sodium channel activation, as reported by Laedermann et al. in 2013 [12]. They observed an increase in current density in addition to a shift of the activation rate toward more hyperpolarized potentials by approximately 3.7 mV [12] and a shift of the average inactivation velocity ($V_{1/2}$ inactivation) toward more depolarized potentials by approximately 1.5 mV [12].

In the context of protein evolution, neighboring amino acids at the PPI recognize each other and lend binding specificity [117]. Thanks to the CDR segments of β3 the presence of the $\beta3$ subunit has a favourable effect on the function of

Table 4 The RMSD of the cryo-EM structure and our three-dimensional binding site model between subunit *α* and *β*3

Reference structure	Computed model	Comparison basis	RMSD [Å]
Crystal structure 7TJ8 with subunits *α* and *β*3	hNa$_v$1.7 with the entire *α*/*β*3 complex	All 1078 pairs of atoms	3
Homology modeling	hNa$_v$1.7 with a part of the *α*/*β*3 complex	Subset of 692 pairs of atoms focusing on the PPI	1
Homology modeling	hNa$_v$1.7 with only DIII of the α/*β*3 complex	All 122 pairs of atoms	2
Homology modeling	hNa$_v$1.7 with only DIII of the *α*/*β*3 complex	Subset of 107 pairs of atoms focusing on the PPI	1

the α subunit with the central pore of the sodium channel. Hence, it is not far-fetched to assume that the stronger the affinity of the CDR segments to the α subunit at the PPI, the greater the electrophysiological effect for the channel.

Our study lends insight about membrane protein/membrane protein interactions, and our findings contribute to the interatomic research, of which we cite two seminal works spanning more than two decades of advances in PPI science [130, 131]. Drug development efforts have been undertaken in the field of human voltage-gated sodium channels, for instance, with channel blockers for skeletal muscle isoform Na$_v$1.4 [132]. Details of recent channel drug research can be found in a seminal review [133].

Conclusion

Since the human Na$_v$1.7 complex between *α* and β3 subunits has not been described experimentally at an atomic scale, its 3D model was generated by homology based on three PDB templates. The resulting crystal structure-like *α*/*β*3 interface was studied in detail by MD.

As a direct finding, we observed that *β*3 subunit interacted with protein segments that modulate the voltage-dependent sodium channel. The three most relevant interactions were documented: (i) overall domain cooperativity at the *α*/*β*3 interface: in the transmembrane area, the interactions that are presented provide stability to the interaction between both proteins. (ii) Charge interaction with VSD in domain DIII: K1287 on *α*/F23 of *β*3 and R1290 on *α*/F23 of *β*3 constitute two pairs of favorable interactions between a variable segment of the Ig-like *β*3 subunit and residues belonging to the S4 segment on *α* subunit. This mechanistic insight explains how this segment moves to allow channel modulation. As a direct consequence, the channel function is modified concerning the kinetics (timing) of the channel opening and closing. (iii) Interactions with complementarity determining regions (CDRs): the Ig-like segment interacts through CDR1 salt bridges with EEDD filter amino acids, K1670 on *α*/E52 of *β*3; K1670 in a E53 and E52 of *β*3; E1672 in *α*/R51 of *β*3 while the interaction through CDR3 is through the formation of a hydrogen bond between E129 and W1354, which also belongs to the EEDD filter at the entrance of the pore. As a last finding, due to this interaction between both subunits, the sodium cation passage through the channel pore from the extracellular entrance to the inner vestibule was simulated in the presence or absence of auxiliary protein *β*3. The computed differences were in perfect keeping with published electrophysiological data.

In addition, the sodium cation passage through the channel pore from the extracellular entrance to the inner vestibule was simulated in the presence or absence of auxiliary protein *β*3. The computed differences were in perfect keeping with published electrophysiological data.

Our study contributes to the emerging field of molecular computational science to study PPI by MD. To complement our study in the inactivated state, future studies could simulate sodium ion passage in the open state of the channel.

Supplementary Information The online version contains supplementary material available at https://doi.org/10.1007/s00894-025-06378-9.

Acknowledgements We thank CONACYT (Mexico) PhD scholarship (Mexico) support numbers 708844 from 2021 to 2024. We feel much beholden to VD and VIEP, respectively, for internal support. We also thank "Laboratorio Nacional de Supercómputo del Sureste de México" between 2021 and 2024 to run MD simulation under the project name: "El rol estructural de la subunidad β3 como regulador del hNa$_v$1.7" and project number: 202103089 C. Vicerrectoría de Investigación y Estudios de Posgrado (VIEP-BUAP, Mexico) (100256733-VIEP2024 project), and the PRODEP Academic Group BUAP-CA-263 (SEP, Mexico).

Author contribution J.E.R.C. and F.V.L carried out the methodology, made the docking and MD calculations, and made data curation, M.E.C. and F.J.M. made data curation, reviewed and edited the manuscript, and funding acquisition, and T.S. made the conceptualization of the manuscript, made data curation, made validation of results, wrote the main manuscript, and project administration. All authors reviewed the manuscript.

Funding This research was funded by Vicerrectoría de Investigación y Estudios de Posgrado (VIEP-BUAP, Mexico) (100256733-VIEP2024 project), and the PRODEP Academic Group (SEP, Mexico) (BUAP-CA-263).

Data availability No datasets were generated or analysed during the current study.

Declarations

Competing of interests The authors declare no competing interests.

Open Access This article is licensed under a Creative Commons Attribution 4.0 International License, which permits use, sharing, adaptation, distribution and reproduction in any medium or format, as long as you give appropriate credit to the original author(s) and the source, provide a link to the Creative Commons licence, and indicate if changes were made. The images or other third party material in this article are included in the article's Creative Commons licence, unless indicated otherwise in a credit line to the material. If material is not included in the article's Creative Commons licence and your intended use is not permitted by statutory regulation or exceeds the permitted use, you will need to obtain permission directly from the copyright holder. To view a copy of this licence, visit http://creativecommons.org/licenses/by/4.0/.

References

1. Katz D, Sindhikara D, DiMattia M, Leffler AE (2021) Potency-enhancing mutations of gating modifier toxins for the voltage-gated sodium channel NaV1.7 can be predicted using accurate free-energy calculations. Toxins 13(3):193. https://doi.org/10.3390/toxins13030193
2. Salvage SC, Rahman T, Eagles DA, Rees JS, King GF, Huang CLH, Jackson AP (2023) The β3-subunit modulates the effect of venom peptides ProTx-II and OD1 on Na_V1.7 gating. J Cell Physiol 238:1354–1367. https://doi.org/10.1002/jcp.31018
3. Pérez-Medina C, Patel N, Robson M, Badar A, Lythgoe MF, Årstad E (2012) Evaluation of a 125I-labelled benzazepinone derived voltage-gated sodium channel blocker for imaging with SPECT. Org Biomol Chem 10:9474–9480. https://doi.org/10.1039/C2OB26695D
4. Xu X, Xu Q, Chen F, Shi J, Liu Y, Chu Y, Wan S, Jiang T, Yu R (2019) Role of the disulfide bond on the structure and activity of m-conotoxin PIIIA in the inhibition of Na_v1.4. RSC Adv 9:668–674. https://doi.org/10.1039/c8ra06103c
5. Salvage SC, Zhu W, Habib ZF, Hwang SS, Irons JR, Huang CLH, Silva JR, Jackson AP (2019) Gating control of the cardiac sodium channel Nav1.5 by its β3-subunit involves distinct roles for a transmembrane glutamic acid and the extracellular domain. J Biol Chem 294:19752–19763. https://doi.org/10.1074/jbc.RA119.010283
6. Isom LL (2001) Sodium channel beta subunits: anything but auxiliary. Neuroscientist 7:42–54. https://doi.org/10.1177/107385840100700108
7. Brackenbury WJ, Isom LL (2011) Na channel β subunits: overachievers of the ion channel family. Front Pharmacol 2:53. https://doi.org/10.3389/fphar.2011.00053
8. Brackenbury WJ, Isom LL (2008) Voltage-gated Na+ channels: potential for beta subunits as therapeutic targets. Expert Opin Ther Targets 12:1191–1203. https://doi.org/10.1517/14728222.12.9.1191
9. Zhu W, Voelker TL, Varga Z, Schubert AR, Nerbonne JM, Silva JR (2017) Mechanisms of noncovalent β subunit regulation of NaV channel gating. J Gen Physiol 149:813–831. https://doi.org/10.1085/jgp.201711802
10. Barro-Soria R, Liin SI, Larsson HP (2017) Using fluorescence to understand β subunit–NaV channel interactions. J Gen Physiol 149:757–762. https://doi.org/10.1085/jgp.201711843
11. Sokolov MV, Henrich-Noack P, Raynoschek C, Franzén B, Larsson O, Main M, Dabrowski M (2018) Co-expression of β subunits with the voltage-gated sodium channel NaV1.7: the importance of subunit association and phosphorylation and their effects on channel pharmacology and biophysics. J Mol Neurosci 2(65):154–166. https://doi.org/10.1007/s12031-018-1082-6
12. Laedermann CJ, Syam N, Pertin M, Decosterd I, Abriel H (2013) β1- and β3-voltage-gated sodium channel subunits modulate cell surface expression and glycosylation of Nav1.7 in HEK293 cells. Front Cell Neurosci 7. https://doi.org/10.3389/fncel.2013.00137
13. Brändén CI, Tooze J (1999) Introduction to protein structure, 2nd edn. New York, Garland Pub
14. Palmisano VF, Gómez-Rodellar C, Pollak H, Cárdenas G, Corry B, Faraji S, Nogueira JJ (2021) Binding of azobenzene and p-diaminoazobenzene to the human voltage-gated sodium channel Nav1.4. Phys Chem Chem Phys 23:1463–9076. https://doi.org/10.1039/D0CP06140A
15. Pan X, Li Z, Huang X, Huang G, Gao S, Shen H, Liu L, Lei J, Yan N (2019) Molecular basis for pore blockade of human Na+ channel Nav1.2 by the μ-conotoxin KIIIA. Science 363:1309–1313. https://doi.org/10.1126/science.aaw2999
16. Li X, Xu F, Xu H, Zhang S, Gao Y, Zhang H, Dong Y, Zheng Y, Yang B, Sun J, Zhang XC, Zhao Y, Jiang D (2022) Structural basis for modulation of human NaV1.3 by clinical drug and selective antagonist. Nat Commun 13:1286. https://doi.org/10.1038/s41467-022-28808-5
17. Pan X, Li Z, Zhou Q, Shen H, Wu K, Huang X, Chen J, Zhang J, Zhu X, Lei J, Xiong W, Gong H, Xiao B, Yan N (2018) Structure of the human voltage-gated sodium channel Nav1.4 in complex with β1. Science 362:eaau2486. https://doi.org/10.1126/science.aau2486
18. Fan X, Huang J, Jin X, Yan N (2023) Cryo-EM structure of human voltage-gated sodium channel Nav1.6. Proc Natl Acad Sci USA 120:e2220578120. https://doi.org/10.1073/pnas.222057812
19. Shen H, Liu D, Wu K, Lei J, Yan N (2019) Structures of human Nav1.7 channel in complex with auxiliary subunits and animal toxins. Science 363:1303–1308. https://doi.org/10.1126/science.aaw2493
20. Berman HM (2000) The protein data bank. Nucleic Acids Res 28:235–242. https://doi.org/10.1093/nar/28.1.235
21. Noland CL, Chua HC, Kschonsak M, Heusser SA, Braun N, Chang T, Tam C, Tang J, Arthur CP, Ciferri C, Pless SA, Payandeh J (2022) Structure-guided unlocking of NaX reveals a non-selective tetrodotoxin-sensitive cation channel. Nat Commun 13:1416. https://doi.org/10.1038/s41467-022-28984-4
22. Wang C, Chung BC, Yan H, Wang HG, Lee SY, Pitt GS (2014) Structural analyses of Ca^{2+}/CaM interaction with NaV channel C-termini reveal mechanisms of calcium-dependent regulation. Nat Commun 5:4896. https://doi.org/10.1038/ncomms5896
23. Mahling R, Fowler CA, Hovey L, Yu L, Gakhar L, Lin Z, Pandey N, Martins T, Shea MA (2016) Ca2+-saturated calmodulin binds tightly to the N-terminal domain of A-type fibroblast growth factor homologous factors. Biophys J 110:109a. https://doi.org/10.1016/j.jbc.2021.100458
24. Namadurai S, Balasuriya D, Rajappa R, Wiemhöfer M, Stott K, Klingauf J, Edwardson JM, Chirgadze DY, Jackson AP (2014) Crystal structure and molecular imaging of the Nav channel β3 subunit indicates a trimeric assembly. J Biol Chem 289:10797–10811. https://doi.org/10.1074/jbc.M113.527994

25. Glass WG, Duncan AL, Biggin PC (2020) Computational investigation of voltage-gated sodium channel β3 subunit dynamics. Front Mol Biosci 7:40. https://doi.org/10.3389/fmolb.2020.00040
26. Yan Z, Zhou Q, Wang L, Wu J, Zhao Y, Huang G, Peng W, Shen H, Lei J, Yan N (2017) Structure of the Nav1.4-β1 complex from electric eel. Cell 170:470-482.e11. https://doi.org/10.1016/j.cell.2017.06.039
27. Li T, Chen J (2018) Voltage-gated sodium channels in drug discovery. InTech. https://doi.org/10.5772/intechopen.78256
28. Sanchez-Sandoval AL, Hernández-Plata E, Gomora JC (2023) Voltage-gated sodium channels: from roles and mechanisms in the metastatic cell behavior to clinical potential as therapeutic targets. Front Pharmacol 14:1206136. https://doi.org/10.3389/fphar.2023.1206136
29. Wang G, Xu L, Chen H, Liu Y, Pan P, Hou T (2023) Recent advances in computational studies on voltage-gated sodium channels: drug design and mechanism studies. WIREs Comput Mol Sci 13:e1641. https://doi.org/10.1002/wcms.1641
30. Nguyen PT, Yarov-Yarovoy V (2022) Towards structure-guided development of pain therapeutics targeting voltage-gated sodium channels. Front Pharmacol 13:842032. https://doi.org/10.3389/fphar.2022.842032
31. Salvage SC, Jeevaratnam K, Huang CLH, Jackson AP (2023) Cardiac sodium channel complexes and arrhythmia: structural and functional roles of the β1 and β3 subunits. J Physiol 601:923–940. https://doi.org/10.1113/JP283085
32. Jiang D, Zhang J, Xia Z (2022) Structural advances in voltage-gated sodium channels. Front Pharmacol 13:908867. https://doi.org/10.3389/fphar.2022.908867
33. Li Z, Wu Q, Yan N (2024) A structural atlas of druggable sites on Nav channels. Channels 18:2287832. https://doi.org/10.1080/19336950.2023.2287832
34. Monastyrnaya MM, Kalina RS, Kozlovskaya EP (2022) The sea anemone neurotoxins modulating sodium channels: an insight at structure and functional activity after four decades of investigation. Toxins 15:8. https://doi.org/10.3390/toxins15010008
35. Clairfeuille T, Cloake A, Infield DT, Llongueras JP, Arthur CP, Li ZR, Jian Y, Martin-Eauclaire MF, Bougis PE, Ciferri C, Ahern CA, Bosmans F, Hackos DH, Rohou A, Payandeh J (2019) Structural basis of α-Scorpion toxin action on Nav channels. Science 363:eaav8573. https://doi.org/10.1126/science.aav8573
36. Guo Y, Luo N, Kang X (2022) Potential mechanism of the Shunaoxin pill for preventing cognitive impairment in type 2 diabetes mellitus. Front Neurol 13:977953. https://doi.org/10.3389/fneur.2022.977953
37. Zhang J, Shi Y, Huang Z, Li Y, Yang B, Gong J, Jiang D (2022) Structural basis for Nav1.7 inhibition by pore blockers. Nat Struct Mol Biol 29:1208–1216. https://doi.org/10.1038/s41594-022-00860-1
38. Zidar N, Tomašič T, Kikelj D, Durcik M, Tytgat J, Peigneur S, Rogers M, Haworth A, Kirby RW (2023) New aryl and acylsulfonamides as state-dependent inhibitors of Nav1.3 voltage-gated sodium channel. Eur J Med Chem 258:115530. https://doi.org/10.1016/j.ejmech.2023.115530
39. Huang G, Liu D, Wang W, Wu Q, Chen J, Pan X, Shen H, Yan N (2022) High-resolution structures of human Nav1.7 reveal gating modulation through α-π helical transition of S6IV. Cell Reports 39:110735. https://doi.org/10.1016/j.celrep.2022.110735
40. Huang X, Jin X, Huang G, Huang J, Wu T, Li Z, Chen J, Kong F, Pan X, Yan N (2022) Structural basis for high-voltage activation and subtype-specific inhibition of human Nav1.8. Proc Natl Acad Sci USA 119:e2208211119. https://doi.org/10.1073/pnas.2208211119
41. Raffo A, Fugacci U, Biasotti S (2023) GEO-Nav: a geometric dataset of voltage-gated sodium channels. Comput Graph 115:285–295. https://doi.org/10.1016/j.cag.2023.06.023
42. Huang G, Wu Q, Li Z, Jin X, Huang X, Wu T, Pan X, Yan N (2022) Unwinding and spiral sliding of S4 and domain rotation of VSD during the electromechanical coupling in Nav1.7. Proc Natl Acad Sci USA 119:e2209164119. https://doi.org/10.1073/pnas.2209164119
43. Liu Y, Bassetto CAZ, Pinto BI, Bezanilla F (2023) Mechanistic reinterpretation of fast inactivation in voltage-gated Na+ channels. Nat Commun 14:5072. https://doi.org/10.1038/s41467-023-40514-4
44. Huang J, Fan X, Jin X, Teng L, Yan N (2023) Dual-pocket inhibition of nav channels by the antiepileptic drug lamotrigine. Proc Natl Acad Sci USA 120:e2309773120. https://doi.org/10.1073/pnas.2309773120
45. Li Y, Yuan T, Huang B, Zhou F, Peng C, Li X, Qiu Y, Yang B, Zhao Y, Huang Z, Jiang D (2023) Structure of human Nav1.6 channel reveals Na+ selectivity and pore blockade by 4,9-anhydro-tetrodotoxin. Nat Commun 14:1030. https://doi.org/10.1038/s41467-023-36766-9
46. Wu Q, Huang J, Fan X, Wang K, Jin X, Huang G, Li J, Pan X, Yan N (2023) Structural mapping of Nav1.7 antagonists. Nat Commun 14:3224. https://doi.org/10.1038/s41467-023-38942-3
47. Seneci L, Mikheyev AS (2024) Sodium channel β subunits—an additional element in animal tetrodotoxin resistance? J Mol Sci 25:1478. https://doi.org/10.3390/ijms25031478
48. González-Cano R, Ruiz-Cantero MC, Santos-Caballero M, Gómez-Navas C, Tejada MÁ, Nieto FR (2021) Tetrodotoxin, a potential drug for neuropathic and cancer pain relief? Toxins 13:483. https://doi.org/10.3390/toxins13070483
49. McMahon KL, Vetter I, Schroeder CI (2024) Voltage-gated sodium channel inhibition by µ-conotoxins. Toxins 16:55. https://doi.org/10.3390/toxins16010055
50. McMahon KL, Tran HNT, Deuis JR, Lewis RJ, Vetter I, Schroeder CI (2020) Discovery, pharmacological characterisation and NMR structure of the novel µ-conotoxin SxIIIC, a potent and irreversible Nav channel inhibitor. Biomedicines 8:391. https://doi.org/10.3390/biomedicines8100391
51. Waxman SG, Cummins TR, Dib-Hajj SD, Black JA (2000) Voltage-gated sodium channels and the molecular pathogenesis of pain: a review. J Rehabil Res Dev 37:517–528
52. Pukkanasut P, Whitt J, Guenter R, Lynch SE, Gallegos C, Rosendo-Pineda MJ, Gomora JC, Chen H, Lin D, Sorace A, Jaskula-Sztul R, Velu SE (2023) Voltage-gated sodium channel Nav1.7 inhibitors with potent anticancer activities in medullary thyroid cancer cells. Cancers 15:2806. https://doi.org/10.3390/cancers15102806
53. Doray A, Lemoine R, Severin M, Chadet S, Lopez-Charcas O, Héraud A, Baron C, Besson P, Monteil A, Pedersen SF, Roger S (2021) The voltage-gated sodium channel beta4 subunit maintains epithelial phenotype in mammary cells. Cells 10:1624. https://doi.org/10.3390/cells10071624
54. Dib-Hajj SD, Cummins TR, Black JA, Waxman SG (2007) From genes to pain: Na v 1.7 and human pain disorders. Trends Neurosci 30:555–563. https://doi.org/10.1016/j.tins.2007.08.004
55. Leźnicka K, Pawlak M, Sawczuk M, Gasiorowska A, Leońska-Duniec A (2023) SCN9A Rs6746030 polymorphism and pain perception in combat athletes and non-athletes. Genes 14:733. https://doi.org/10.3390/genes14030733
56. MacDonald DI, Sikandar S, Weiss J, Pyrski M, Luiz AP, Millet Q, Emery EC, Mancini F, Iannetti GD, Alles SRA, Zhao J, Cox JJ, Brownstone RM, Zufall F Wood JN (2020) The mechanism of analgesia in Nav1.7 null mutants. bioRxiv. https://doi.org/10.1101/2020.06.01.127183

57. MacDonald DI, Sikandar S, Weiss J, Pyrski M, Luiz AP, Millet Q, Emery EC, Mancini F, Iannetti GD, Alles SRA (2021) A central mechanism of analgesia in mice and humans lacking the sodium channel Nav1.7. Neuron 109:1497-1512.e6. https://doi.org/10.1016/j.neuron.2021.03.012
58. Alexandrou AJ, Brown AR, Chapman ML, Estacion M, Turner J, Mis MA, Wilbrey A, Payne EC, Gutteridge A, Cox PJ, Doyle R, Printzenhoff D, Lin Z, Marron BE, West C, Swain NA, Storer RI, Stupple PA, Castle NA, Hounshell JA, Rivara M, Randall A, Dib-Hajj SD, Krafte D, Waxman SG, Patel MK, Butt RP, Stevens EB (2016) Subtype-selective small molecule inhibitors reveal a fundamental role for Nav1.7 in nociceptor electrogenesis, axonal conduction and presynaptic release. PLoS ONE 11:e0152405. https://doi.org/10.1371/journal.pone.0152405
59. Rogers M, Tang L, Madge DJ, Stevens EB (2006) The role of sodium channels in neuropathic pain. Semin Cell Dev Biol 17:571–581. https://doi.org/10.1016/j.semcdb.2006.10.009
60. Dib-Hajj SD, Black JA, Waxman SG (2009) Voltage-gated sodium channels: therapeutic targets for pain. Pain Med 10:1260–1269. https://doi.org/10.1111/j.1526-4637.2009.00719.x
61. Schmalhofer WA, Calhoun J, Burrows R, Bailey T, Kohler MG, Weinglass AB, Kaczorowski GJ, Garcia ML, Koltzenburg M, Priest BT (2008) ProTx-II, a selective inhibitor of Nav1.7 sodium channels, blocks action potential propagation in nociceptors. Mol Pharmacol 74:1476–1484. https://doi.org/10.1124/mol.108.047670
62. Grubinska B, Chen L, Alsaloum M, Rampal N, Matson D, Yang C, Taborn K, Zhang M, Youngblood B, Liu D, Galbreath E, Allred S, Lepherd M, Ferrando R, Kornecook TJ, Lehto SG, Waxman SG, Moyer BD, Dib-Hajj S, Gingras J (2019) Rat NaV1.7 loss-of-function genetic model: deficient nociceptive and neuropathic pain behavior with retained olfactory function and intra-epidermal nerve fibers. Mol Pain 15:174480691988184. https://doi.org/10.1177/1744806919881846
63. Shields SD, Deng L, Reese RM, Dourado M, Tao J, Foreman O, Chang JH, Hackos DH (2018) Insensitivity to pain upon adult-onset deletion of Nav1.7 or its blockade with selective inhibitors. J Neurosci 38:10180–10201. https://doi.org/10.1523/JNEUROSCI.1049-18.2018.44
64. Hoffmann T, Sharon O, Wittmann J, Carr RW, Vyshnevska A, Col RD, Nassar MA, Reeh PW, Weidner C (2018) Nav1.7 and pain: contribution of peripheral nerves. Pain 159:496–506. https://doi.org/10.1097/j.pain.0000000000001119
65. Flinspach M, Xu Q, Piekarz AD, Fellows R, Hagan R, Gibbs A, Liu Y, Neff RA, Freedman J, Eckert WA, Zhou M, Bonesteel R, Pennington MW, Eddinger KA, Yaksh TL, Hunter M, Swanson RV, Wickenden AD (2017) Insensitivity to pain induced by a potent selective closed-state Nav1.7 inhibitor. Sci Rep 7:39662. https://doi.org/10.1038/srep39662
66. Vetter I, Deuis JR, Mueller A, Israel MR, Starobova H, Zhang A, Rash LD, Mobli M (2017) Nav1.7 as a pain target - from gene to pharmacology. Pharmacol Ther 172:73–100. https://doi.org/10.1016/j.pharmthera.2016.11.015
67. Sun S, Jia Q, Zenova AY, Wilson MS, Chowdhury S, Focken T, Li J, Decker S, Grimwood ME, Andrez JC, Hemeon I, Sheng T, Chen CA, White A, Hackos DH, Deng L, Bankar G, Khakh K, Chang E, Kwan R, Lin S, Nelkenbrecher K, Sellers BD, DiPasquale AG, Chang J, Pang J, Sojo L, Lindgren A, Waldbrook M, Xie Z, Young C, Johnson JP, Robinette CL, Cohen CJ, Safina BS, Sutherlin DP, Ortwine DF, Dehnhardt CM (2019) Identification of selective acyl sulfonamide-cycloalkylether inhibitors of the voltage-gated sodium channel (Nav) 1.7 with potent analgesic activity. J Med Chem 62:908–927. https://doi.org/10.1021/acs.jmedchem.8b01621
68. Birch PJ, Dekker LV, James IF, Southan A, Cronk D (2004) Strategies to identify ion channel modulators: current and novel approaches to target neuropathic pain. Drug Discov Today 9:410–418. https://doi.org/10.1016/S1359-6446(04)03043-0
69. Capurro A, Thornton J, Cessac B, Armstrong L, Sernagor E (2019) On the role of Nav1.7 sodium channels in chronic pain: an experimental and computational study. bioRxiv. https://doi.org/10.1101/871236
70. Lin L, Li K, Tian B, Jia M, Wang Q, Xu C, Xiong L, Wang Q, Zeng Y, Wang P (2022) Two novel functional mutations in promoter region of SCN3B gene associated with atrial fibrillation. Life 12:1794. https://doi.org/10.3390/life12111794
71. Villa-Diaz F, Lopez-Nunez S, Ruiz-Castelan JE, Salinas-Stefanon EM, Scior T (2020) Chemometric models of differential amino acids at the Navα and Navβ interface of mammalian sodium channel isoforms. Molecules 25:3551. https://doi.org/10.3390/molecules25153551
72. Scior T, Paiz-Candia B, Islas ÁA, Sánchez-Solano A, Millan-Perez Peña L, Mancilla-Simbro C, Salinas-Stefanon EM (2015) Predicting a double mutant in the twilight zone of low homology modeling for the skeletal muscle voltage-gated sodium channel subunit beta-1 (Nav1.4 β1). Comput Struct Biotechnol J 13:229–240. https://doi.org/10.1016/j.csbj.2015.03.005
73. Islas AA, Sánchez-Solano A, Scior T, Millan-Perez Peña L, Salinas-Stefanon EM (2013) Identification of Navβ1 residues involved in the modulation of the sodium channel Nav1.4. PLoS ONE 8(12):e81995. https://doi.org/10.1371/journal.pone.0081995
74. Sánchez-Solano A, Islas AA, Scior T, Paiz-Candia B, Millan-Perez Peña L, Salinas-Stefanon EM (2017) Characterization of specific allosteric effects of the Na+ channel β1 subunit on the Nav1.4 isoform. Eur Biophys J 46:485–494. https://doi.org/10.1007/s00249-016-1193-3
75. Körner J, Meents J, Machtens JP, Lampert A (2018) β1 subunit stabilises sodium channel Nav1.7 against mechanical stress. J Physiol 596(12):2433–2445. https://doi.org/10.1113/JP275905
76. Baroni D, Moran O (2015) On the multiple roles of the voltage gated sodium channel β1 subunit in genetic diseases. Front Pharmacol 6:108. https://doi.org/10.3389/fphar.2015.00108
77. Baroni D, Picco C, Moran O (2017) Mutation E87Q of the β1-subunit impairs the maturation of the cardiac voltage-dependent sodium channel. Sci Rep 7:10683. https://doi.org/10.1038/s41598-017-10645-y
78. Johnson D, Montpetit ML, Stocker PJ, Bennett ES (2004) The sialic acid component of the β1 subunit modulates voltage-gated sodium channel function. J Biol Chem 279(43):44303–44310. https://doi.org/10.1074/jbc.M408900200
79. Angsutararux P, Zhu W, Voelker TL, Silva JR (2021) Molecular pathology of sodium channel beta-subunit variants. Front Pharmacol 12:761275. https://doi.org/10.3389/fphar.2021.761275
80. Bouza AA, Isom LL (2018) Voltage-gated sodium channel β subunits and their related diseases. Springer Cham 246:423–450. https://doi.org/10.1007/164_2017_48
81. Bouza AA, Edokobi N, Hodges SL, Pinsky AM, Offord J, Piao L, Zhao YT, Lopatin AN, Lopez-Santiago LF, Isom LL (2021) Sodium channel β1 subunits participate in regulated intramembrane proteolysis-excitation coupling. JCI Insight 6(3):e141776. https://doi.org/10.1172/jci.insight.141776
82. Madeira F, Pearce M, Tivey ARN, Basutkar P, Lee J, Edbali O, Madhusoodanan N, Kolesnikov A, Lopez R (2022) Search and sequence analysis tools services from EMBL-EBI in 2022. Nucleic Acids Res 50:W276–W279. https://doi.org/10.1093/nar/gkac240
83. Sievers F, Wilm A, Dineen D, Gibson TJ, Karplus K, Li W, Lopez R, McWilliam H, Remmert M, Söding J, Thompson JD, Higgins DG (2011) Fast, scalable generation of high-quality protein multiple sequence alignments using Clustal Omega. Mol Syst Biol 7:539. https://doi.org/10.1038/msb.2011.75

84. Sievers F, Higgins DG (2018) Clustal Omega for making accurate alignments of many protein sequences. Protein Sci 27:135–145. https://doi.org/10.1002/pro.3290
85. Sievers F, Higgins DG (2014) Clustal Omega. Curr Protoc Bioinform 48. https://doi.org/10.1002/0471250953.bi0313s48
86. Pedretti A, Mazzolari A, Gervasoni S, Fumagalli L, Vistoli G (2021) The VEGA suite of programs: an versatile platform for cheminformatics and drug design projects. Bioinformatics 37:1174–1175. https://doi.org/10.1093/bioinformatics/btaa774
87. Webb B, Sali A (2016) Comparative protein structure modeling using MODELLER. Curr Protoc Bioinform 54:5–6. https://doi.org/10.1002/cpbi.3
88. Fiser A, Do RK, Sali A (2000) Modeling of loops in protein structures. Protein Sci 9:1753–1773. https://doi.org/10.1110/ps.9.9.1753
89. Martí-Renom MA, Stuart AC, Fiser A, Sánchez R, Melo F, Šali A (2000) Comparative protein structure modeling of genes and genomes. Annu Rev Biophys Biomol Struct 29:291–325. https://doi.org/10.1146/annurev.biophys.29.1.291
90. Šali A, Blundell TL (1993) Comparative protein modelling by satisfaction of spatial restraints. J Mol Biol 234:779–815. https://doi.org/10.1006/jmbi.1993.1626
91. Pettersen EF, Goddard TD, Huang CC, Couch GS, Greenblatt DM, Meng EC, Ferrin TE (2004) UCSF Chimera?A visualization system for exploratory research and analysis. J Comput Chem 25:1605–1612. https://doi.org/10.1002/jcc.20084
92. The UniProt Consortium (2023) UniProt: the universal protein knowledgebase in 2023. Nucleic Acids Res 51:D523–D531. https://doi.org/10.1093/nar/gkac1052
93. Lindahl A, Hess S VD (2021) GROMACS 2021.4 Source Code. https://zenodo.org/records/5636567. Accessed 28 Apr 2025
94. Studer G, Biasini M, Schwede T (2014) Assessing the local structural quality of transmembrane protein models using statistical potentials (QMEANBrane). Bioinformatics 30:i505–i511. https://doi.org/10.1093/bioinformatics/btu457
95. Benkert P, Biasini M (2011) Schwede T (2011) Toward the estimation of the absolute quality of individual protein structure models. Bioinformatics 27:343–350. https://doi.org/10.1093/bioinformatics/btq662
96. Briones R, Blau C, Kutzner C, de Groot BL, Aponte-Santamaría C (2019) GROmaρs: a GROMACS-based toolset to analyze density maps derived from molecular dynamics simulations. Biophys J 116:4–11. https://doi.org/10.1016/j.bpj.2018.11.3126
97. Lindahl A, Hess S VD (2021) GROMACS 2021.4 Source Code. https://zenodo.org/records/5636567
98. Lindahl A, Hess S VD (2021) GROMACS 2021.4 Manual. https://doi.org/10.5281/ZENODO.5636522
99. Johansson MU, Zoete V, Michielin O, Guex N (2012) Defining and searching for structural motifs using DeepView/Swiss-PdbViewer. BMC Bioinformatics 13:173. https://doi.org/10.1186/1471-2105-13-173
100. Guex N, Peitsch MC (1996) wiss-PdbViewer: a fast and easy-to-use PDB viewer for Macintosh and PC. Protein Data Bank Quaterly Newsletter 77:7. https://doi.org/10.1002/elps.1150181505
101. Yan Y, Zhang D, Zhou P, Li B, Huang SY (2017) HDOCK: a web server for protein-protein and protein-DNA/RNA docking based on a hybrid strategy. Nucleic Acids Res 45(W1):W365–W373
102. Yan Y, Wen Z, Wang X, Huang SY (2017) Addressing recent docking challenges: a hybrid strategy to integrate template-based and free protein-protein docking. Proteins 85:497–512
103. Honorato RV, Trellet ME, Jiménez-García B, Schaarschmidt JJ, Giulini M, Reys V, Koukos PI, Rodrigues JPGLM, Karaca E, van Zundert GCP, Roel-Touris J, van Noort CW, Jandová Z, Melquiond ASJ, Bonvin AMJJ (2024) The HADDOCK2.4 web server: a leap forward in integrative modelling of biomolecular complexes. Nature Prot 19:3219–3241
104. Honorato RV, Koukos PI, Jimenez-Garcia B, Tsaregorodtsev A, Verlato M, Giachetti A, Rosato A, Bonvin AMJJ (2021) Structural biology in the clouds: the WeNMR-EOSC ecosystem. Frontiers Mol Biosci 8:729513
105. Jo S, Kim T, Iyer VG, Im W (2008) CHARMM-GUI: a web-based graphical user interface for CHARMM. J Comput Chem 29:1859–1865. https://doi.org/10.1002/jcc.20945
106. Brooks BR, Brooks CL, Mackerell AD, Nilsson L, Petrella RJ, Roux B, Won Y, Archontis G, Bartels C, Boresch S, Caflisch A, Caves L, Cui Q, Dinner AR, Feig M, Fischer S, Gao J, Hodoscek M, Im W, Kuczera K, Lazaridis T, Ma J, Ovchinnikov V, Paci E, Pastor RW, Post CB, Pu JZ, Schaefer M, Tidor B, Venable RM, Woodcock HL, Wu X, Yang W, York DM, Karplus M (2009) CHARMM: the biomolecular simulation program. J Comput Chem 30:1545–1614. https://doi.org/10.1002/jcc.21287
107. Lee J, Cheng X, Swails JM, Yeom MS, Eastman PK, Lemkul JA, Wei S, Buckner J, Jeong JC, Qi Y, Jo S, Pande VS, Case DA, Brooks CL, MacKerell AD Jr, Klauda JB, Im W (2016) CHARMM-GUI input generator for NAMD, GROMACS, AMBER, OpenMM, and CHARMM/OpenMM simulations using the CHARMM36 additive force field. J Chem Theory Comput 12:405–413. https://doi.org/10.1021/acs.jctc.5b00935
108. Lomize MA, Pogozheva ID, Joo H, Mosberg HI, Lomize A (2012) OPM database and PPM web server: resources for positioning of proteins in membranes. Nucleic Acids Res 40:D370–D376. https://doi.org/10.1093/nar/gkr703
109. Tieleman DP, Forrest LR, Sansom MS, Berendsen HJ (1998) Lipid properties and the orientation of aromatic residues in OmpF, influenza M2, and alamethicin systems: molecular dynamics simulations. Biochemistry 37(50):17554–17561. https://doi.org/10.1021/bi981802y
110. Humphrey W, Dalke A, Schulten K (1996) VMD: visual molecular dynamics. J Mol Graph 14:33–38. https://doi.org/10.1016/0263-7855(96)00018-5
111. Turner PJ (2005) XMGRACE. Version 5(1):19
112. Arnittali M, Rissanou AN, Harmandaris V (2019) Structure of biomolecules through molecular dynamics simulations. Procedia Computer Science 156:69–78. https://doi.org/10.1016/j.procs.2019.08.181
113. Jumper J, Evans R, Pritzel A, Green T, Figurnov M, Ronneberger O, Tunyasuvunakool K, Bates R, Žídek A, Potapenko A, Bridgland A, Meyer C, Kohl SAA, Ballard AJ, Cowie A, Romera-Paredes B, Nikolov S, Jain R, Adler J, Back T, Petersen S, Reiman D, Clancy E, Zielinski M, Steinegger M, Pacholska M, Berghammer T, Bodenstein S, Silver D, Vinyals O, Senior AW, Kavukcuoglu K, Kohli P, Hassabis D (2021) Highly accurate protein structure prediction with AlphaFold. Nature 596:583–589. https://doi.org/10.1038/s41586-021-03819-2
114. Filipe HAL, Loura LMS (2022) Molecular dynamics simulations: advances and applications. Molecules 27:2105. https://doi.org/10.3390/molecules27072105
115. Maiorov VN, Crippen GM (1994) Significance of root-mean-square deviation in comparing three dimensional structures of globular proteins. J Mol Biol 2:625–634
116. Kufareva I, Abagyan R (2012) Methods of protein structure comparison. Methods Mol Biol 857:231–257
117. Ghadimi M, Khalifeh K, Heshmati E (2017) Neighbor effect and local conformation in protein structures. Amino Acids 49:1641–1646. https://doi.org/10.1007/s00726-017-2463-9
118. Infield DT, Rasouli A, Galles GD, Chipot C, Tajkhorshid E, Ahern CA (2021) Cation-π interactions and their functional roles in membrane proteins. J Mol Biol 433:167035. https://doi.org/10.1016/j.jmb.2021.167035

119. Gallivan JP, Dougherty DA (1999) Cation-π interactions in structural biology. Proc Natl Acad Sci USA 96:9459–9464. https://doi.org/10.1073/pnas.96.17.9459
120. Xia X, Xie Z (2002) Protein structure, neighbor effect, and a new index of amino acid dissimilarities. Mol Biol Evol 19:58–67. https://doi.org/10.1093/oxfordjournals.molbev.a003982
121. Schmidt T, Situ AJ, Ulmer TS (2016) Structural and thermodynamic basis of proline-induced transmembrane complex stabilization. Sci Rep 6:29809. https://doi.org/10.1038/srep29809
122. Morales P, Hurst DP, Reggio PH (2017) Methods for the development of in silico GPCR models. In: Methods in enzymology. Elsevier 593:405–448. https://doi.org/10.1016/bs.mie.2017.05.005
123. Visiers I, Braunheim BB, Weinstein H (2000) A Protocol for numerical evaluation of helix distortions by proline. Protein Eng Des Sel 13:603–606. https://doi.org/10.1093/protein/13.9.603
124. Wilman HR, Shi J, Deane CM (2014) Helix kinks are equally prevalent in soluble and membrane proteins. Proteins 82:1960–1970. https://doi.org/10.1002/prot.24550
125. Jacob J, Duclohier H, Cafiso DS (1999) The role of proline and glycine in determining the backbone flexibility of a channel-forming peptide. Biophys J 76:1367–1376. https://doi.org/10.1016/S0006-3495(99)77298-X
126. Groome JR (2014) The voltage sensor module in sodium channels. Springer 221:7–31
127. Sula A, Booker J, Ng LCT, Naylor CE, DeCaen PG, Wallace BA (2017) The complete structure of an activated open sodium channel. Nat Commun 8:14205. https://doi.org/10.1038/ncomms14205
128. Vascon F, Gasparotto M, Giacomello M, Cendron L, Bergantino E, Filippini F, Righetto I (2020) Protein electrostatics: from computational and structural analysis to discovery of functional fingerprints and biotechnological design. Comput Struct Biotechnol J 18:1774–1789. https://doi.org/10.1016/j.csbj.2020.06.029
129. Ramos RH, Ferreira CD, Simao A (2024) Human protein–protein interaction networks: a topological comparison review. Heliyon 5:2405–8440. https://doi.org/10.1016/j.heliyon.2024.e27278
130. Janin J, Miller S, Chothia C (1998) Surface, subunit interfaces and interior of oligomeric proteins. J Mol Biol 204:155–164. https://doi.org/10.1016/0022-2836(88)90606-7
131. Chakrabarti P, Janin J (2002) Dissecting protein–protein recognition sites. Proteins 47:334–343. https://doi.org/10.1002/prot.10085
132. De Bellis M, Boccanegra B, Cerchiara AG, Imbrici P, De Luca A (2023) Blockers of skeletal muscle Nav1.4 channels: from therapy of myotonic syndrome to molecular determinants of pharmacological action and back. Int J Mol Sci 24:857. https://doi.org/10.3390/ijms24010857
133. Gualdani R, Cavalluzzi MM, Lentini G (2016) Recent trends in the discovery of small molecule blockers of sodium channels. Curr Med Chem 23(22):2289–2332. https://doi.org/10.2174/0929867323666160517121458

Publisher's Note Springer Nature remains neutral with regard to jurisdictional claims in published maps and institutional affiliations.